An adaptive multiresolution semi-intrusive scheme for UQ in compressible fluid problems

Abgrall, Rémi ; Congedo, Pietro Marco ; Geraci, Gianluca ; Iaccarino, Gianluca

Abstract: This paper deals with the introduction of a multiresolution strategy into the semi-intrusive scheme, recently introduced by the authors, aiming to propagate uncertainties in unsteady compressible fluid applications. The mathematical framework of the multiresolution setting is presented for the cell-average case, and the coupling with the semi-intrusive scheme is described from both the theoretical and algorithmic point-of-view. Some reference test cases are performed to demonstrate the convergence properties and the efficiency of the overall scheme: the linear advection problem for both smooth and discontinuous initial conditions, the inviscid Burgers equation, and an uncertain shock tube problem obtained by modifying the well-known Sod shock problem. For all the cases, the convergence curves are computed with respect to semi-analytical (exact) solutions. In the case of the shock tube problem, an original technique to obtain a reference highly-accurate numerical stochastic solution has also been developed.

DOI: https://doi.org/10.1002/fld.4030

INTERNATIONAL JOURNAL FOR NUMERICAL METHODS IN FLUIDS
Int. J. Numer. Meth. Fluids 2013; **00**:1–43
Published online in Wiley InterScience (www.interscience.wiley.com). DOI: 10.1002/fld

An adaptive multiresolution semi-intrusive scheme for UQ in compressible fluid problems

R. Abgrall[1], P.M. Congedo[2], G. Geraci*[2,3] and G. Iaccarino[3]

[1] *Institut für Mathematik, Universität Zürich, Winterthurerstrasse 190, CH-8057 Zürich, Switzerland*
[2] *INRIA Bordeaux–Sud-Ouest, 200 Avenue de la Vieille Tour, 33405 Talence Cedex, France*
[3] *Mechanical Engineering, Flow Physics and Computational Engineering Department, Stanford University, 488 Escondido Mall, CA 94305-3035, Stanford, USA.*

SUMMARY

This paper deals with the introduction of a multiresolution strategy into the semi-intrusive scheme, recently introduced by the authors, aiming to propagate uncertainties in unsteady compressible fluid applications. The mathematical framework of the multiresolution setting is presented for the cell-average case and the coupling with the semi-intrusive scheme is described from both the theoretical and algorithmic point-of-view. Some reference test cases are performed to demonstrate the convergence properties and the efficiency of the overall scheme: the linear advection problem for both smooth and discontinuous initial conditions, the inviscid Burgers equation and an uncertain shock tube problem obtained by modifying the well-known Sod shock problem. For all the cases, the convergence curves are computed with respect to semi-analytical (exact) solutions. In the case of the shock tube problem, an original technique to obtain a reference highly-accurate numerical stochastic solution has also been developed. Copyright © 2013 John Wiley & Sons, Ltd.

Received . . .

KEY WORDS: Finite volume, Uncertainty Quantification, linear advection, Burgers equation, Euler equations, shock tube

1. INTRODUCTION AND MOTIVATION

In recent years, the scientific numerical community faced a new challenge: the analysis and propagation of uncertain parameters through the numerical models. In particular, the attention is focused not only on the accurate numerical solution of the equations, but also on the effect of uncertain parameters (on boundary or initial conditions and/or on the model) on the variability of the numerical solution.

Among the non-intrusive approaches, *i.e.* where uncertainties are propagated by making multiple calls to a deterministic code, several methods are commonly employed: Monte Carlo techniques [1], collocation [2] and the non-intrusive Galerkin projection methods. These last methods have been introduced for the first time by Ganem and Spanos [3] for the analysis of structural dynamics systems and has been generalized by Xiu and Karniadakis [4] to general probability distributions. Actually, the non-intrusive Galerkin projection represents the state-of-the art of the stochastic analysis for systems with a smooth response surface due to its spectral convergence property.

The Galerkin projection is also the most used technique in order to handle intrusively the uncertainty propagation into a numerical code. In practice, this means that it is possible to obtain an

*Correspondence to: Mechanical Engineering, Flow Physics and Computational Engineering Department, Stanford University, 488 Escondido Mall, CA 94305-3035, Stanford, USA.

equivalent set of governing equations for the coefficients of a truncated polynomial representation of the quantities of interest [5]. The number of equations is related to the number of coefficients employed in the polynomial expansion, and the numerical code should be deeply modified. In many cases, the required theoretical re-formulation of the mathematical problem reduces the generality of the approach, thus requiring *ad hoc* solvers [6]. More recently, Abgrall and co-workers proposed a novel semi-intrusive (SI) approach that extend in a straightforward and natural way, the representation of the variables in the physical space also along the stochastic space [7, 8]. This approach leads to very flexible schemes able to handle whatever forms of probability density function even time varying and discontinuous. One of the prominent advantage of this kind of approach is the possibility to extend, in an easier way, an existing deterministic numerical formulation to its stochastic counterparts.

Following the general idea of a semi-intrusive propagation of the uncertainties, recently, the authors [9, 10, 11] introduced a point-value setting in the multiresolution (MR) framework to represent data in the stochastic space. The multiresolution representation of data permits to increase the efficiency of the numerical code for the solution of stochastic partial differential equations. The idea of introducing the MR representation of data, in the context of stochastic problem, is not totally new. In [5], a multiresolution basis is employed to represent the solution of a partial differential equations after fixing the physical coordinates. This representation is very efficient but limited to the case where the stochastic representation is used at a fixed physical location. To overcome this issue, more recently, Tryoen et al. introduced in [6] a multiresolution wavelets representation in the context of intrusive Galerkin projections. However, the Galerkin approach presented remains very problem-dependent. In fact, using a Roe-type solver demands the computation of the eigenstructure of the Roe matrix explicitly; this can be very complex. Moreover, *ad hoc* entropy fix should be adopted, thus increasing the numerical cost associated to the representation of discontinuous solution [12]. This original approach has been further improved to obtain a more efficient scheme employing a multiresolution adaptive strategy [13]. However, this approach is limited by the spatial and time discretization accuracy (only first order) that could dominate the overall accuracy. Moreover, the approach proposed in [9, 10, 11] has the advantage to remain very general, not limited from the order of the spatial and time discretization, from the probability density function (that can be even discontinuous and time varying) and, eventually, from the geometry of the stochastic space in the case of multidimensional problems.

In this paper, the MR method, already introduced as the Truncate and Encode (TE) framework in [14], is extended to the cell-average framework and the representation is integrated in the semi-intrusive scheme [7, 8]. Thanks to its intrinsic capability to handle discontinuous responses, the semi-intrusive method represents a promising alternative to the Galerkin projection techniques for all the applications where the system is dominated by moving shock/high-gradient regions, as for example in computational fluid dynamics for transonic flows.

In this paper, the aim is to demonstrate the advantages of the introduction of a real-time adaptivity in the stochastic space driven by the MR, which makes possible to follow the evolution of the solution in the overall physical and stochastic space. This is shown by comparing the accuracy, at a fixed computational cost, with and without the adaptivity. Different reference test-cases are performed for which the reference solution can be obtained by means of analytical or semi-analytical approaches.

The remaining part of the paper is organized as follows. In Section 2, the mathematical setting for the stochastic differential equation, here of interest, is given. Section 3 illustrates the multi-resolution framework adopted, the TE [14], where a cell-average setting is chosen and the non-liner high-order reconstruction is performed. In particular, the Truncate and Encode algorithm is presented in Section 3.2, where the representation of the discrete data is obtained moving from the coarsest level towards the finest. The semi-intrusive scheme is briefly sketched in Section 4 where the formulation is detailed for the MUSCL-Hancock method. The overall formulation of the adaptive semi-intrusive scheme, obtained modifying the baseline SI by the introduction of the MR setting, presented in Section 5. Several numerical results are presented in Section 6. In particular, the introduction of the adaptive representation of data in the stochastic space is demonstrated to

DOI: 10.1002/fld

improve the spatial convergence and to cure the staircase approximation phenomenon with respect to an equivalent semi-intrusive not adapted solution. Concluding remarks are drawn in Section 7.

2. UNCERTAINTY QUANTIFICATION FOR PARTIAL DIFFERENTIAL EQUATIONS

In this section, the mathematical setting used for the UQ analysis in the context of partial differential equations is briefly introduced. In the following, the focus is on a generic output of interest $u(\mathbf{x}, t, \boldsymbol{\xi}(\theta))$ depending on the physical space $\mathbf{x} \in \Omega \subset \mathbb{R}^{n_d}$ and the time $t \in T \subset \mathbb{R}^+$. The randomness is introduced in the system by means of $\boldsymbol{\xi}$, which is a random vector. The output of interest u can be a conserved variable (or primitive, or another flow variable), or vector of variables, of a system of conservation laws, hence it is governed by an algebraic or differential operator $\mathcal{L}$ with a source term $\mathcal{S}$:

$$\mathcal{L}(\mathbf{x}, t, \boldsymbol{\xi}(\theta); u(\mathbf{x}, t, \boldsymbol{\xi}(\theta))) = \mathcal{S}(\mathbf{x}, t, \boldsymbol{\xi}(\theta)). \tag{1}$$

Initial and boundary conditions, which could depend on the random vector $\boldsymbol{\xi}$, should be provided for a well-posed problem. Both the operators $\mathcal{L}$ and the source term $\mathcal{S}$ are defined on the domain $\Omega \times T \times \Xi$. The random vector $\boldsymbol{\xi}$ can be defined providing a measure space (Θ, Σ, μ), where Σ is its $\sigma-$algebra of events and μ a probability measure; the $\mathbb{R}^d-$valued random variable $\boldsymbol{\xi}$ specifies a set of events with a corresponding probability, *i.e.* $\boldsymbol{\xi}(\theta) : \theta \to \Xi \subset \mathbb{R}^d$. The space $\Xi \stackrel{\text{def}}{=} \boldsymbol{\xi}(\Theta)$, the image of the random vector, is also the support of the probability density function $p(\boldsymbol{\xi})$.

One of the aims of UQ analysis is to find the statistical characterization of the solution $u(\mathbf{x}, t, \boldsymbol{\xi})$; for instance this goal can be reached through the evaluation of the moments of the solution or its probability distribution. Assuming $u(\mathbf{x}, t, \boldsymbol{\xi}) \in L^2(\Xi, p)$ for any $(\mathbf{x}, t) \in \Omega \times T$, the expected value and variance can be computed as follows:

$$\begin{aligned} \mathcal{E}(u, \mathbf{x}, t) &= \int_\Xi u(\mathbf{x}, t, \boldsymbol{\xi}) p(\boldsymbol{\xi}) \mathrm{d}\boldsymbol{\xi} \\ \mathrm{Var}(u, \mathbf{x}, t) &= \int_\Xi \left(u(\mathbf{x}, t, \boldsymbol{\xi}) - \mathcal{E}(u)\right)^2 p(\boldsymbol{\xi}) \mathrm{d}\boldsymbol{\xi}. \end{aligned} \tag{2}$$

3. THE CELL-AVERAGE MULTIRESOLUTION SETTING

In this section, the multiresolution framework in a cell-averaged representation of data is presented.

The Truncate and Encode (TE) framework, previously presented in other works [15, 10, 11], is generalized here to handle cell average data. Moreover, the original TE approach is extended by yielding a non-linear high-order multiresolution framework. This is coupled, for the first time, with the semi-intrusive (SI) scheme proposed in [7, 8]. The final long-term goal is to improve the efficiency of the original SI approach by curing the so-called curse of dimensionality [16]. This is done by means of the multiresolution representation of data and exploiting an adaptive refinement/coarsening strategy in the coupled physical-stochastic space. Note that, in this paper, the terms data and solution are used without any distinction. In the context of data analysis, data refer to a collection of realizations, while the term solution is usually employed to define the result of the numerical discretization of an equation, as for example a partial differential equation. Roughly speaking, data analysis algorithms deal with information already available, while in the present paper, the interest is in the solution of partial differential equations with uncertainty. Anyway, it is always possible to identify a process in which the information are obtained (the discretization step described in the following) by a numerical discretization of the equations and, a second one, in which the information (now available) are handled by data analysis techniques. In the following, the terms are used without any particular distinction being considered equivalent for our purpose.

On the contrary with respect to the works [15, 10, 11], here the TE approach aims at mimicking the general feature of the SI scheme; this aspect naturally leads to a finite volume like representation of data, which is a cell-average discretization. Another relevant difference is contained in the

DOI: 10.1002/fld

discretization step: in the point-value setting the numerical equations are solved for a specific set of points in the overall space $\Omega \times T \times \Xi$, while, in the cell-average approach coupled with the SI, the discretization step consists into accounting for all the flux contributions in each cell built in the coupled physical/stochastic space (see also Section 4.2 for further details).

The multiresolution representation of data can be considered, as pointed out by Aràndiga and Donat in [17], as a rearrangement of the information in a set of discrete data representing different resolution levels. This rearrangement of data, within the addition of a truncation procedure, could yield a reduction of the computational cost and of the memory usage associated to the representation/calculation and memorization of discrete data. The Harten multiresolution framework can be viewed as a more general framework with respect to the classical wavelets framework in which the hierarchical representation of data is obtained by means of a functional basis relying on a dilating equation and a so called mother wavelet. As presented in [18], the dilating equation in a general space can be difficult to solve, especially for domains of complex geometries. The Harten framework, which has inspired the TE algorithm, is capable to avoid the solution of a dilating equation obtaining a local polynomial basis for general geometries with, eventually, data-dependent strategies for the representation of data. Dealing with hyperbolic problems in presence of uncertainties can lead to the propagation of discontinuities/high-gradients regions in the physical-stochastic space. The possibility to employ non-linear algorithms to circumvent the issues related to the data reconstruction, in the neighboring of these regions, is well known in the CFD community [19, 20] as well in the signal processing community [21]. The Harten framework, by exploiting the locality of the information, constitutes a very powerful and flexible tool for introducing a more general framework for the representation of data in the context of the numerical solution of partial differential equations for compressible fluid problems. This is the main source of inspiration for this work. However, as it will be evident in the following of this section, the application of the multiresolution setting as presented in the seminal works of Harten and collaborators [22, 23, 24], is not possible in this context. However, some of the mathematical tools developed in the Harten' multiresolution context, can be extended, with some minor efforts, to the more general case of spaces characterized by a probability measure μ instead of a Lebesgue measure. This task is accomplished in Section 3.1, where the mathematical tools are recalled and extended to the probability measure case. These generalized tools, introduced in Section 3.1, can be employed to develop the TE algorithm, presented in Section 3.2. This algorithm shares, with the Harten' framework (and in general with the multigrid algorithms) a main idea: exploiting the information on the coarser resolution levels to obtain in an efficient way, *i.e.* by means of a reduced computational cost, the solution at the finest resolution. In the present paper, this task is performed by developing a recursive mesh refinement on the different resolution levels, exploiting the information collected at the previous (coarser) resolution levels. The peculiarity of this approach is to avoid any kind of operation, from the finer level to the coarser one, aiming to maximize the efficiency of the algorithm. The only operation, in which the solution at the finer resolution level is employed (locally) to inform the coarser level, is the so-called Discretize-Agglomerate-Decimate (DAD) algorithm which is described in Section 3.3. The non-linear (conservative) reconstruction of the data is recalled in Section 3.4, where the ENO procedure employed is also introduced.

3.1. Generalization of the mathematical tools to generic probability measure

Two building blocks can be defined in the multiresolution setting [18, 25]: a discretization operator $\mathcal{D}_k$ and a reconstruction operator $\mathcal{R}_k$. These two operators allows to define, in a unique way, two other operators working on data rearrangement between different resolution levels. These discrete operators, transferring information between consecutive levels k (higher resolution) and $k-1$ (lower resolution), are the operators of decimation D_k^{k-1} and prediction P_{k-1}^k. In the following, the operator involving the continuous space ($\mathcal{D}_k$ and $\mathcal{R}_k$) are denoted by calligraphic fonts, while the discrete spaces (D_k^{k-1} and P_{k-1}^k) are denoted by standard fonts. The TE framework relies on the same building blocks, $\mathcal{D}_k$ and $\mathcal{R}_k$, of the Harten multiresolution framework, which are introduced to guide, in *real time*, the refinement/coarsening of the stochastic space taking into account an explicitly dependence on the physical and time locations. Note that, in the TE algorithm,

DOI: 10.1002/fld

the representation of the solution is adapted, following the regularity of the solution by employing information at the same time step (from the coarser resolution level). On the contrary, in the Harten's framework, at each time step the mesh is generated by employing only information at the previous time step and a CFL based conditions [22]. In the TE algorithm, the adaptive procedure is employed at the same time of the computation in order to prevent the computation of useless information and not just at the end of the procedure to yield the new time step. Moreover, in terms of memory requirements, *i.e.* the quantity of information to store in order to recover the solution on the finest level, the TE algorithm can recover the classical Harten multiresolution properties, as demonstrated in [15]. In the following, we deal with the representation of a generic function f (defined on the stochastic space). The main assumption here is the possibility to obtain a discrete value for f without defining the numerical discretization which leads to this evaluation. The application of the TE algorithm, in which the discretization step is performed by means of the SI scheme [7, 8], leads to the adaptive SI (aSI) approach for UQ and it is presented in Section 5.

In the classical MR cell-average framework, $f \in \mathcal{F}$ where $\mathcal{F}$ is the functional space of the absolutely integrable functions $\mathcal{F} = L^1(\Xi)$. However, in the context of UQ, $\mathcal{F}$ is identified with L^2 dealing with functions with finite variance. Introducing the probability density function $p(\boldsymbol{\xi})$, the following measure can be derived

$$\mathrm{d}\mu(\boldsymbol{\xi}) = p(\boldsymbol{\xi})\mathrm{d}\boldsymbol{\xi}. \tag{3}$$

The introduction of the measure (3) allows mimicking the classical framework in which the measure is a Lebesgue measure with a formal analogy between the two frameworks.

If the stochastic space is represented by means of a non-overlapping tessellation

$$\Xi = \bigcup_{j=1}^{N_\xi} \Xi_j, \quad \text{with} \quad \Xi_i \cap \Xi_j = 0 \quad \text{if} \quad i \neq j. \tag{4}$$

the measure of each element of the tessellation can be found as follows

$$\mu(\Xi_j) = \int_{\Xi_j} \mathrm{d}\mu(\boldsymbol{\xi}). \tag{5}$$

Moreover, even if not employed in the present work, the previous definition naturally permits to take into account for pdfs with a support having non finite Lebesgue measure, because the measure of each element is always defined over $]0, 1[$.

A set of discrete operators of discretization $\{\mathcal{D}_k\}_{k=0}^{L}$, each of them defined on a vectorial space of finite dimension, can be introduced

$$\mathcal{D}_k : \quad \mathcal{F} \to V_k \quad \text{with} \quad \dim(V_{k+1}) > \dim(V_k) = J_k. \tag{6}$$

The sequence $\{\mathcal{D}_k\}_{k=0}^{L}$ has to be nested according to the following properties:

- $\mathcal{D}_k$ is onto
- the null space of each level includes the null space associated to the previous resolution level $\mathcal{N}(\mathcal{D}_k) \subset \mathcal{N}(\mathcal{D}_{k+1})$.

These properties reflect in the following relation between discretization operators

$$\mathcal{D}_{k+1}(f) = 0 \Rightarrow \mathcal{D}_k(f) = 0 \quad \forall f \in \mathcal{F}. \tag{7}$$

Such an operator on the k-th level can be defined over the j-th cell Ξ_j^k as

$$(\mathcal{D}_k f)_j \stackrel{\text{def}}{=} \frac{1}{\mu(\Xi_j^k)} \int_{\Xi_j^k} f(\boldsymbol{\xi})\mathrm{d}\mu(\boldsymbol{\xi}) = v_j^k. \tag{8}$$

Thanks to the onto property of each operator $\mathcal{D}_k$, the reconstruction operator $\mathcal{R}_k$ can be defined as its right-inverse

$$\mathcal{R}_k : \quad V_k \to \mathcal{F}. \tag{9}$$

DOI: 10.1002/fld

The reconstruction operator is not required to be linear and this makes the Harten multiresolution more general with respect to the wavelet framework [26].

The two operators $\mathcal{D}_k$ and $\mathcal{R}_k$ should satisfy a consistency relationship between them

$$(\mathcal{D}_k\mathcal{R}_k)(v) = v \quad \forall v \in V_k, \tag{10}$$

thus implying $\mathcal{D}_k\mathcal{R}_k = \mathrm{I}_k$ where I_k is the identity operator on V_k.

This relation is fundamental for searching a consistent reconstruction procedure. Originally, Harten introduced the reconstruction of $\mathcal{R}_k$ by employing the concept of reconstruction via primitive function. In practice, the cell-averaged function is replaced by a point valued function that corresponds to its primitive in the nodes of the mesh. A more convenient approach satisfying (10), *i.e.* a conservative reconstruction in a finite volume context, can be adopted by following Abgrall and Sonar [27], even for multidimensional problems on unstructured meshes [25]. Fixing a polynomial degree of reconstruction r, a stencil $\mathcal{S}_j^k$ of cells with cardinality $s = s(r) = \mathrm{card}(\mathcal{S}_j^k)$ can be fixed. On each stencil $\mathcal{S}_j^k$, a polynomial $\mathcal{P}_j^k(\boldsymbol{\xi}; f)$ of degree r can be constructed. The admissibility of this stencil obeys a Vandermonde condition (see for further details [27]). Supposing the stencils admissible, the conditions to satisfy for the computation of $\mathcal{P}_j^k$ are

$$\mathcal{D}_k(\mathcal{P}_j^k(\boldsymbol{\xi}; f))_l = \mathcal{D}_k(f)_l, \quad \forall l \in \mathcal{S}_j^k. \tag{11}$$

Thus, the reconstruction operator $\mathcal{R}_k$ is identified as the union of all the polynomials $\mathcal{P}_j^k$ defined on all the cells Ξ_j^k.

The decimation operator D_k^{k-1} can be defined as a linear mapping between V_k onto V_{k-1}:

$$\mathrm{D}_k^{k-1}: \quad V_k \to V_{k-1}, \tag{12}$$

where

$$\mathrm{D}_k^{k-1}v^k = \mathcal{D}_{k-1}f \in V_{k-1} \quad \forall v^k = \mathcal{D}_k f \in V_k. \tag{13}$$

By an agglomeration (splitting) procedure, for a generic mesh, even unstructured, it is always possible to obtain a less (higher) resolution level. To each cell Ξ_j^k, at the lower resolution level, corresponds a number of cells ($\bar{l}_c$) at the higher resolution level. To preserve the nested character between levels, the following property between elements of the tessellation, defined at adjacent resolution level, should hold:

$$\Xi_j^k = \bigcup_{l}^{\bar{l}_c} \Xi_l^{k+1}. \tag{14}$$

In the following, without loss of generality, $\bar{l}_c = 2$ is assumed. This case, the dyadic splitting, appears naturally for the 1D case of equally divided cells between levels in the case of regular nested meshes (this is always possible employing the measure introduced in (3)).

In this case, the decimation operator (see figure 2) can be obtained as follows

$$\begin{aligned}(\mathrm{D}_k^{k-1}v^k)_j = (\mathrm{D}_k^{k-1}\mathcal{D}_k f)_j = (\mathcal{D}_{k-1}f)_j &= \frac{1}{\mu(\Xi_j^{k-1})}\int_{\Xi_j^{k-1}} f(\boldsymbol{\xi})\mathrm{d}\mu(\boldsymbol{\xi}) \\ &= \frac{1}{\mu(\Xi_j^{k-1})}\left(\mu(\Xi_{2j}^k)(\mathcal{D}_k f)_{2j} + \mu(\Xi_{2j-1}^k)(\mathcal{D}_k f)_{2j-1}\right).\end{aligned} \tag{15}$$

Moreover, the prediction P_{k-1}^k allows to approximate the set of data v^k from v^{k-1}. The relation

$$v^k = \mathcal{D}_k f \approx \mathcal{D}_k(\mathcal{R}_{k-1}v^{k-1}) \tag{16}$$

leads to the definition of the prediction operator P_{k-1}^k between discrete data on successive resolution levels as

$$\mathrm{P}_{k-1}^k \stackrel{\mathrm{def}}{=} \mathcal{D}_k\mathcal{R}_{k-1}: \quad V^{k-1} \to V^k. \tag{17}$$

DOI: 10.1002/fld

The prediction operator P_{k-1}^{k} is obtained following the definition (17) and using first the reconstruction procedure (11) for the level $k-1$th, and then applying the discretization operator $\mathcal{D}_k(\mathcal{P}_j^{k-1})$ relative to the level k.

A consistency property can be defined, $\mathrm{D}_k^{k-1}\mathrm{P}_{k-1}^{k} = \mathrm{I}_k$, that follows from

$$v^{k-1} = \mathrm{D}_k^{k-1}v^k = \mathrm{D}_k^{k-1}\mathcal{D}_k f = \mathrm{D}_k^{k-1}\mathcal{D}_k\mathcal{R}_{k-1}v^{k-1} = \mathrm{D}_k^{k-1}\mathrm{P}_{k-1}^{k}v^{k-1}. \tag{18}$$

Until now, how obtaining discrete data from the continuous functional space $\mathcal{F}$ by means of $\mathcal{D}_k$ and the reverse operation by means of $\mathcal{R}_k$ has been presented. Moreover, the discrete data can be used to transfer information between adjacent resolution levels by means of the discrete operators P_{k-1}^{k} and D_k^{k-1}. The remaining element to introduce is the prediction error e^k which can be employed, for each resolution level, to verify the quality of the data representation (driving the refinement if needed).

The prediction error e^k is defined as

$$e^k \stackrel{\text{def}}{=} v^k - \mathrm{P}_{k-1}^{k}v^{k-1} \tag{19}$$

and it satisfies (from the consistency property (18))

$$\mathrm{D}_k^{k-1}e^k = \mathrm{D}_k^{k-1}(v^k - \mathrm{P}_{k-1}^{k}v^{k-1}) = v^{k-1} - v^{k-1} = 0, \tag{20}$$

i.e. it is in the null space of the decimation operator $e^k \in \mathcal{N}(\mathrm{D}_k^{k-1})$. The last relation can be exploited to obtain, by means of the rank theorem

$$\dim(V_k) = \dim(\mathcal{N}(\mathrm{D}_k^{k-1})) + \dim(V_{k-1}) \rightarrow \dim(\mathcal{N}(\mathrm{D}_k^{k-1})) = \dim(V_k) - \dim(V_{k-1}) = J_k - J_{k-1}, \tag{21}$$

the number of its linear independent components. The $J_k - J_{k-1}$ linear independent coordinates of e^k are called wavelets or details d^k. Note that, in the following, the term wavelet is employed to indicate the linear independent components of the error vector as historically done in the classical multiresolution context [22, 23, 24, 25]. However, the wavelet may refer also to the orthonormal and bi-orthogonal basis itself as in [28]. With this meaning, wavelets has been also adopted in the solution of stochastic partial differential equations as, for instance, in [5, 13]. Hereafter, the wavelets is intended in the Harten' sense: linear independent component of the error vector. The definition of $J_k - J_{k-1}$ linear independent components of the error vector is based only on the cardinality of the two spaces J_k and J_{k-1} and it does not reflect the strategy adopted for the mesh refinement. This point is clarified in the following, where the link between the wavelets d^k and the error e^k vector is presented for the case of a dyadic splitting of each cell (as adopted in the numerical example) (see also the relation (30)).

It is a common practice in multiresolution theory (as for instance in [22, 23, 18]) the introduction of a truncation procedure, *i.e.* a wavelet is considered to be significant only if higher than a threshold. The problem statement is the following: given a sequence of scale coefficients or wavelets for a fixed level d^k and assigned a level dependent tolerance criterion ε_k, to obtain $\hat{d}^k = \left\{\hat{d}_j^k\right\}_{j=1}^{J_k - J_{k-1}}$ according to

$$\hat{d}_j^k = \mathrm{tr}(d_j^k, \varepsilon_k) = \begin{cases} 0 & |d_j^k| \leq \varepsilon_k \\ d_j^k & \text{otherwise.} \end{cases} \tag{22}$$

Different choices exist in literature for the threshold parameter ε_k: a level independent choice $\varepsilon_k = \varepsilon$ or a dependent criterion $\varepsilon_k = \varepsilon/2^{L-k}$. Harten proposed [24] to modify the *encoding* procedure in order to preserve the following condition

$$||v^L - \hat{v}^L|| \leq C\varepsilon, \tag{23}$$

with a constant C and measured in some norms as L^1 and L^∞. However, in the present work, the aim is to reproduce the function by starting from the coarsest level towards the finest one. This

DOI: 10.1002/fld

aspect implies that the stability requirement is naturally satisfied if the convergence of the discrete representation, on the finest level, is attained. A deeper discussion regarding this point is reported in [15] for the point-value framework.

To conclude the presentation of the mathematical tools of the multiresolution setting, table I is reported to resume the fundamental operators, their functional space definitions and symbols. Moreover, in table II, the relations between the operator are resumed.

Operator	Symbol	Space
Discretization	$\mathcal{D}_k$	$\mathcal{F} \to V_k$
Reconstruction	$\mathcal{R}_k$	$V_k \to \mathcal{F}$
Prediction	P_{k-1}^{k}	$V_{k-1} \to V_k$
Decimation	D_{k}^{k-1}	$V_k \to V_{k-1}$

Table I. Operators in the multiresolution setting. For each operator, the symbol and the functional space are reported.

$\diagdown$	$\mathcal{D}_k$	$\mathcal{R}_k$	P_{k-1}^{k}	D_{k}^{k-1}
$\mathcal{D}_k$	$\mathbb{I}$	Inverse	Defining	Defining
$\mathcal{R}_k$	Inverse	$\mathbb{I}$	Defining	–
P_{k-1}^{k}	Defined by	Defined by	$\mathbb{I}$	Reverse
D_{k}^{k-1}	Defined by	–	Reverse	$\mathbb{I}$

Table II. Relations between operators in the multiresolution setting. The table must be read by rows. Inverse and reverse are employed to characterize relations between operators which are the mathematical inverse or only perform the reverse operation between the discrete space of definition.

3.2. A one-time truncate and encode cell-average representation

In this section, the truncate and encode TE algorithm is described in the case of cell-average quantities. The pivotal idea of the algorithm is to identify in the prediction error e^k (at a certain kth level), a measure of the quality of the discrete data.

From classical interpolation results (see for instance [29]), the (polynomial) interpolation error diminishes, moving from a coarser level to a finer one, with a rate determined by the local regularity of the function and by the order of interpolation. This result has been also explicitly shown in [15] for the TE algorithm in the point value setting.

On the contrary, in presence of discontinuities, the error remains constant and of the order $\mathcal{O}[1]$. This means that, starting from the knowledge of a fine level k (using the discretization operators $\mathcal{D}_k$), the recursive combinations of prediction operations via the operators P_{k-1}^{k} and evaluations of the error e^k permits to compute the regions, where the discrete representation of the solution satisfies a certain accuracy criterion. In particular, if the accuracy criterion is chosen as the threshold ε and it is enforced at each resolution level by means of the truncation procedure (22), the TE algorithm produces a set of data $\{v^k\}_{k=0}^{L}$, which satisfies the estimation (23), playing the role of the compressed data $\hat{v}^L$; further details can be found in [15], where the result is discussed for the point value setting.

The algorithm starts with the definition of the coarsest level of resolution $k = 1$. On this level, the discretization operator is applied by obtaining the discrete data v^1: $v^1 = \mathcal{D}_1 f$. By decimation, it is also possible to obtain the discrete data on the level $k = 0$, knowing only v^1:

$$v^0 = \mathrm{D}_1^0 v^1. \tag{24}$$

DOI: 10.1002/fld

An *encoding* step, analogous to what is normally done in the classical MR, is then completed by computing the linear independent coefficients d^k of e^k for $k = 1$. The other components of the error vector e^k are instead evaluated by knowing d^k. The truncation is applied on d^1 with respect to the threshold ε, defined by the user, and to the relation $\varepsilon_k = \varepsilon_k(\varepsilon, k)$:

$$\hat{d}^1 = \mathrm{tr}(d^1, \varepsilon_k). \tag{25}$$

This operation relies on the knowledge of the finest level ($k = L$), *i.e.* the number of refinements separating the current kth level from the finest one, where the threshold is equal to ε (see (22)). The integer $k = L$ is assigned to the finest level, if the coarsest is marked as $k = 0$ and at each refinement k is increased by one.

The data d^1 are analyzed in order to locate the regions of the domain, where the accuracy of the prediction, via P^k_{k-1}, is not adequate. This is accomplished in a very simple way after the truncation, by identifying the non-zero wavelets $\hat{d}^1_j$. At each non-zero (truncated) wavelets, corresponds a region where the knowledge of the solution is not accurate enough under the criterion used in the truncation (25). Then, further information should be added.

By knowing v^2 and v^1, an *encoding* step is performed by computing d^2 and their truncated counterpart $\hat{d}^2$ by using (22). The algorithm is repeated until reaching the finest level L or a full satisfactory prediction, *i.e.* $\hat{d}^k_j = 0$ for all $j = 1, \ldots, J_k - J_{k-1}$.

In principle, two different strategies can be adopted for generating the tessellation. The first one relies on the generation of a finer resolution level $k + 1$ by dividing each cell belonging to k. The explicit evaluation of the cell-average values is performed via the discretization operator only for the cells corresponding to non well-resolved regions. On the contrary, for all the other cells belonging to $k + 1$, the *decoding* is applied. This strategy has the advantage to represent always the data over equally spaced tessellation (at least in terms of the measure $\mathrm{d}\mu$ (3)). However, the number of cells to handle can be very high even for 1D applications. To overcome this issue, it is also possible to refine the tessellation only in correspondence of regions marked as not satisfactory. If a generic cell belonging to the kth level, marked by an active wavelet, is divided following (14), the tessellations $\mathcal{G}^k$ and $\mathcal{G}^{k+1}$ remain nested. A sketch of the two refinement procedures is reported in figure 1.

In the following, it is assumed that, providing a tessellation $\mathcal{G}^k$ and the linear (truncated) independent coordinates of the error vector, $\hat{d}^k$, the finer level $\mathcal{G}^{k+1}$ is obtained by dividing only the cells marked as significant (see figure 1 on the right). The procedure described above is referred in the following, as a *Level Advancement* step. It is now possible to describe the TE algorithm for the case of 1D stochastic space. Some preliminary operations are performed:

- Generation of two nested meshes $\mathcal{G}^k$ for $k = 0, 1$ (0 is the coarsest mesh):

$$\mathcal{G}^k = \left\{\Xi^k_j\right\}_{j=1}^{J_k} \quad \text{where} \quad \Xi^k_j = [\xi^k_{j-1}, \xi^k_j]. \tag{26}$$

The case of probability density function with finite Lebesgue measure for its support (see Section 2), is addressed, and a topological tessellation for the mesh can be obtained, *i.e.* each cell within the same resolution level has the same Lebesgue measure equal to $1/J_k$. Otherwise, the set of meshes can be built on a nested sequence of cells having the same probability measure. In the case of a non-uniform pdf still having a bounded support, the generation of the finer level can rely, *a priori*, on both a subdivision based on Lebesgue measure or probability measure. In the case of non-uniform probability distributions, it is not possible to satisfy, at the same time, an equal subdivision of the cell in terms of its Euclidean distance (Lebesgue measure) and probability measure. Even if the case of non-uniform distributions has not been analyzed in this paper, it is quite intuitive that the probability measure should be preferred. Anyway, in the case of uniform distributions, the two subdivision strategies lead to identical results.

DOI: 10.1002/fld

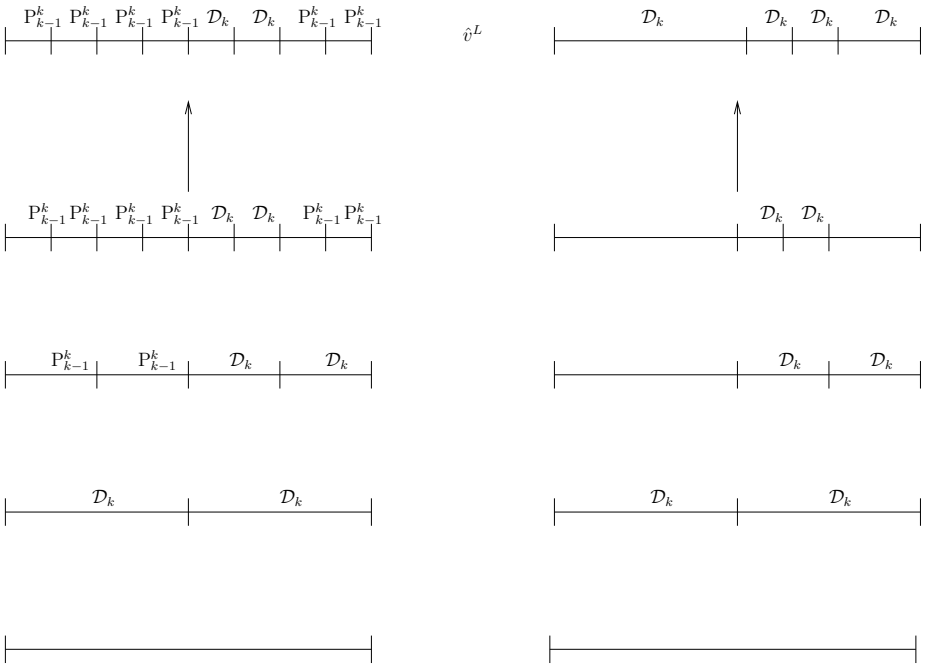

Figure 1. Two different level advancing techniques. On the left, the approach with the splitting of the entire resolution level (employing recursively the *decoding* step via the prediction operator P_{k-1}^k); on the right the approach based on the refinement dependent data-structure. On the top, the final tessellation is represented in both cases.

- Definition of the operators $\mathcal{D}_k$, $\mathcal{R}_k$, D_k^{k-1} and P_{k-1}^k according to §3:

$$\begin{cases} (\mathcal{D}_k f(\xi))_j = \dfrac{1}{\mu(\Xi_j^k)} \displaystyle\int_{\Xi_j^k} f(\xi) p(\xi) \mathrm{d}\xi \\ \mathcal{R}_k : (\mathcal{D}_k \mathcal{P}_j^k)_l = (\mathcal{D}_k f(\xi))_l \quad \text{with} \quad l \in \mathcal{S}_j^k, \quad \mathcal{R}_k(\xi) = \mathcal{P}_j^k(\xi) \quad \forall \xi \in \Xi_j^k \\ (\mathrm{P}_{k-1}^k v^{k-1})_j = (\mathcal{D}_k \mathcal{R}_{k-1} v^{k-1})_j = \dfrac{1}{\mu(\Xi_j^k)} \displaystyle\int_{\Xi_j^k} \mathcal{R}_{k-1} v^{k-1} p(\xi) \mathrm{d}\xi. \end{cases} \tag{27}$$

The decimation operator can be defined, when the topological relation between the cells at two different resolution levels is known. Let us consider the situation sketched in figure 2. It is assumed that the cells generated by the splitting of Ξ_j^{k-1} are named Ξ_{2j-1}^k and Ξ_{2j}^k, even if this numeration does not correspond to the index j of the generating stochastic cell at the lower resolution level. The indexes numeration in figure 2 is exactly matched, only if all the cells are divided (see figure 1) from a resolution level to the higher one. In this case, the dimensions of the spaces of the two levels $k-1$ and k are related by the relation $J_k/J_{k-1} = 2$. In the following, the abstract indexes $2j$ and $2j-1$ are employed to highlight the dependence of the two cells, at level k, from the generating cell Ξ_j^{k-1}. However, the indexes should always be intended in the sense described above. When a cell is divided to obtain the higher resolution level (see figure 2), the measures of the three cells are related satisfying:

$$\begin{cases} \mu(\Xi_j^{k-1}) = \mu(\Xi_{2j-1}^k) + \mu(\Xi_{2j}^k) \\ \mu(\Xi_{2j-1}^k) = \mu(\Xi_{2j}^k). \end{cases} \tag{28}$$

Then, the decimation operator is simply obtained as a convex combination

$$(\mathrm{D}_k^{k-1} v^k)_j = v_j^{k-1} = \frac{1}{\mu(\Xi_j^{k-1})} \left(\mu(\Xi_{2j}^k) v_{2j}^k + \mu(\Xi_{2j-1}^k) v_{2j-1}^k \right) \tag{29}$$

DOI: 10.1002/fld

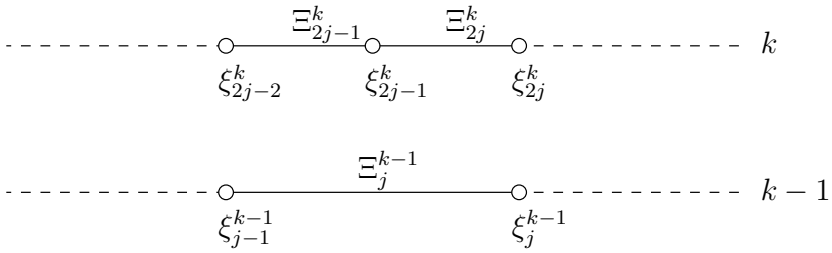

Figure 2. Example of 1D stochastic nested meshes for the cell-average setting decimation procedure.

- Setting a proper threshold ε and a proper relation for $\varepsilon_k = \varepsilon_k(\varepsilon, k; L)$
- Discretization of the level $k = 1$: $(v^1) = (\mathcal{D}_1 f)$;
- Decimation of the discrete data v^1 to obtain $(v^0) = (\mathrm{D}_1^0 v^1)$.

The TE algorithm for cell-average setting in 1D stochastic space can be explicitly written as:

Algorithm 1: Truncate and Encode algorithm for the cell average setting in 1D stochastic space.

while $2 \leq k \leq L$ **do**
  for $j = 1, \ldots, J_{k-2}$ **do**
    Encoding:
    $(d^{k-1})_j = v^{k-1}_{2j} - (\mathrm{P}^{k-1}_{k-2} v^{k-2})_{2j} = v^{k-1}_{2j} - \left(\frac{1}{\mu(\Xi^{k-1}_{2j})} \int_{\Xi^{k-1}_{2j}} \mathcal{R}_{k-2} v^{k-2} p(\xi) \mathrm{d}\xi \right)$
    Truncation: $\hat{d}^{k-1}_j = \mathrm{tr}(d^{k-1}_j, \varepsilon_{k-1})$
  end
  Level Advancement: $(\mathcal{G}^{k-1}, \hat{d}^{k-1}) \to \mathcal{G}^k$
  for $j = 1, \ldots, J_{k-1}$ **do**
    if $\hat{d}^{k-1}_j > 0$ **then**
      Discretization: $v^k_{2j} = (\mathcal{D}_k f)_{2j} = \frac{1}{\mu(\Xi^k_{2j})} \int_{\Xi^k_{2j}} f(\xi) p(\xi) \mathrm{d}\xi$;
      Discretization: $v^k_{2j-1} = (\mathcal{D}_k f)_{2j-1} = \frac{1}{\mu(\Xi^k_{2j-1})} \int_{\Xi^k_{2j-1}} f(\xi) p(\xi) \mathrm{d}\xi$;
    end
  end
end

The nested sequence of the meshes implies that the error vector e^k can be represented by means of only its independent components, the wavelets d^k. It is always possible to write the error e^k, recalling its definition (19) and the nested property of the discretization operator (15), as follows

$$\begin{aligned} e^k_{2j-1} &= v^k_{2j-1} - (\mathrm{P}^k_{k-1} v^{k-1})_{2j-1} \\ &= \frac{1}{\mu(\Xi^k_{2j-1})} \left(\mu(\Xi^{k-1}_j) v^{k-1}_j - \mu(\Xi^k_{2j}) v^k_{2j} \right) - \frac{1}{\mu(\Xi^k_{2j-1})} \left(\mu(\Xi^{k-1}_j) v^{k-1}_j - \mu(\Xi^k_{2j}) (\mathrm{P}^k_{k-1} v^{k-1})_{2j} \right) \\ &= \frac{\mu(\Xi^k_{2j})}{\mu(\Xi^k_{2j-1})} \left(\mathrm{P}^k_{k-1} v^{k-1})_{2j} - v^k_{2j} \right) = -\frac{\mu(\Xi^k_{2j})}{\mu(\Xi^k_{2j-1})} d^k_j . \end{aligned} \tag{30}$$

Note that the first loop should be performed in order to compute the *wavelets* d^k_j, while the second loop is performed over the whole set of cells belonging to the resolution level. In particular, the error vector component is compared to the threshold, for deciding whether the discretization via the model evaluation is necessary. In the second loop, in the case of a nested sequence, with a splitting based on the probability measure, the local error is equal to the *wavelet* computed over the same cell Ξ^{k-1}_j (see equation (30)). Therefore, the truncated wavelet is exactly equal to the truncated component of the error.

DOI: 10.1002/fld

In the classical multiresolution framework, the first step is the *encoding* procedure moving from the finest level to the coarsest. Thereafter, the explicit evaluation of the function f is performed only at the finest level, while the other levels are obtained by agglomeration. On the contrary, in the TE algorithm, the encoding step is performed (at the same time) proceeding from the coarsest level. When a higher resolution level is added, *i.e* k, the function should be explicitly evaluated via the discretization operator $\mathcal{D}_k$. Moreover, using conditional expectations by holding the relation (14) between cells at different resolution levels, can influence the numerical accuracy and efficiency of the algorithm. A specific procedure for the regularization of the numerical data should be introduced. The numerical regularization is done by means of the Discetrize Agglomerate Decimate (DAD) algorithm, which is presented in the following section. It is important to remark that the introduction of the DAD algorithm is a peculiarity of the TE algorithm (in the cell average framework) with respect to the classical MR framework, and it does not introduce an adding computational cost. Another key element, peculiar of the TE for preserving the algorithmic efficiency, is the discretization step, which involves a quadrature. This point is of paramount importance, because (14) implies that some information at level k have already been computed. These information should be exploited, at the higher resolution level $k+1$, to preserve the total number of degrees-of-freedom. This point is also pointed out in the following section.

3.3. Preserving the accuracy and efficiency: the DAD algorithm and the choice of the quadrature

The TE algorithm has been successfully applied in [9, 10, 11] in the point-values framework, without requiring any particular cure to preserve both accuracy and efficiency of the scheme. The last statement implies that, in the point values context, the TE algorithm is very similar to the Algorithm 1, obviously by substituting the discretization step with point values evaluations. If considering conditional expectations instead of point-values evaluations can seem straightforward, it requires a special attention if the aim is to preserve the accuracy and the efficiency of the algorithm.

The need for a regularization of the numerical data can be shown by means of a very simple example. For instance, let define the function $f(\xi) = \sin(\pi\xi)$ with $\xi \simeq \mathcal{U}(0,1)$. If two resolution levels are employed, it is possible to define $\Xi^0 = [0,1]$, $\Xi^1_L = [0, \frac{1}{2}]$ and $\Xi^1_R = [\frac{1}{2}, 1]$, for which $\mu(\Xi^0) = \mu(\Xi^1_L) + \mu(\Xi^1_R) = 2\frac{1}{2} = 1$. Moreover, the function f is symmetric with respect to $\xi = \frac{1}{2}$, as it is the case for $p(\xi)$, thus the following relation between the conditional expectations holds (see also (29)): $\mathbb{E}(f \,|\, \Xi^0) = \frac{1}{2}\left(\mathbb{E}(f \,|\, \Xi^1_L) + \mathbb{E}(f \,|\, \Xi^1_R)\right) = \mathbb{E}(f \,|\, \Xi^1_L)$. The previous relation is exact, but in the TE algorithm the three conditional expectations are evaluated numerically and independently each other. For instance, if a two nodes Gauss quadrature is employed for evaluating the conditional expectations, it is easy to verify: $\mathbb{E}(f \,|\, \Xi^0) \approx 0.61619$, and $\mathbb{E}(f \,|\, \Xi^1_L) = \mathbb{E}(f \,|\, \Xi^1_R) \approx 0.63565$, which both differ of 3.20% and 0.15%, respectively, with respect to the analytical result $\mathbb{E}(f \,|\, \Xi_j) = 0.63662$. From a practical point-of-view, relations (29) and (30) are both invalidated. However, in this case, the computation of a higher resolution level is needed if the error on the coarser level, $k = 0$ in this example, is larger than the proper threshold. A new level, thus the conditional expectations $\mathbb{E}(f \,|\, \Xi^1_L)$ and $\mathbb{E}(f \,|\, \Xi^1_R)$, should be computed; the new values can be exploited to fulfill the (29) by updating the corresponding value of $\mathbb{E}(f \,|\, \Xi^0)$. The effect of the fulfillment of the relation (29) is twofold: the error vector can be represented by only its linear independent components, the wavelets, following (30). Moreover, when a polynomial reconstruction of order greater than zero is selected, *i.e.* $card(\mathcal{S}^k_j) > 1$ in (11) (see also Section 3.4 for the high-order non-linear case), the updated value of a cell at the coarser level allows to increase the accuracy of the polynomial reconstruction $\mathcal{P}^k_j$, that is useful for the definition of the reconstruction operator P^k_{k-1} (17) via $\mathcal{R}_k$. The procedure described above can be generalized by the introduction of a numerical regularization algorithm, the Discetrize Agglomerate

DOI: 10.1002/fld

Decimate (DAD) algorithm. Thus, the DAD algorithm consists in the following operations

Algorithm 2: DAD algorithm.

Discretization:

$$v_{2j}^k = \frac{1}{\mu(\Xi_{2j}^k)} \int_{\Xi_{2j}^k} f(\xi)p(\xi)\mathrm{d}\xi \; ;$$
$$v_{2j-1}^k = \frac{1}{\mu(\Xi_{2j-1}^k)} \int_{\Xi_{2j-1}^k} f(\xi)p(\xi)\mathrm{d}\xi \; ;$$

Agglomeration:

$$\mu(\Xi_j^{k-1}) = \mu(\Xi_{2j-1}^k) + \mu(\Xi_{2j}^k) \; ;$$

Decimation:

$$(\mathrm{D}_k^{k-1} v^k)_j = v_j^{k-1} = \frac{1}{\mu(\Xi_j^{k-1})} \left(\mu(\Xi_{2j}^k) v_{2j}^k + \mu(\Xi_{2j-1}^k) v_{2j-1}^k\right)$$

The DAD algorithm should be always performed before the *Encoding* in the TE algorithm 2. On the contrary, during the preliminary operations, when moving from $k = 1$ to $k = 0$, the DAD regularization is not required (because this is already the decimation step of a multiresolution algorithm). Roughly speaking, the DAD algorithm is necessary because, proceeding from the coarser levels towards the finer ones, implies that the new values are, level by level, more accurate that the previous ones. This is never the case of the classical MR framework, because the *encoding* step is always performed after the (recursive) *decimation* from the finest resolution level. The consistency of the information contained at each level, for the classical MR framework, has the same cost of the explicit evaluation of the solution, at the finest resolution level. Moreover, the introduction of the DAD algorithm is a peculiarity of the cell-average framework, while the point-value setting does not require any similar procedure, because two successive levels are constituted by a set of points in the intersection of the two discrete spaces and a point evaluation of the function does not depend on the resolution level.

Concerning the previous example, using Gauss quadrature formula, six point evaluations of $\sin(\pi\xi)$ are required, two per cell, to obtain the three cell values. If compared with a classical MR decimation step, this last requires just the four points at the last resolution level. In this form, the algorithm is not efficient because the information at the two levels are computed in a complete independent way even if they can be related. Recovering the efficiency of the TE algorithm is possible by means of the choice of an opportune quadrature rule. The family of Newton-Cotes formula, employing only equally spaced points, is the best choice in terms of computational cost; this family of quadrature rule is both nested and based on equally spaced points. For instance, the three points quadrature rule of Newton Cotes, known also as the Cavalieri-Simpson rule, is employed in this work:

$$\int_a^b f(\xi)\mathrm{d}\mu(\xi) = \int_a^b f(\xi)p(\xi)\mathrm{d}\xi \approx \frac{b-a}{6}\left(f(a)p(a) + 4f\left(\frac{a+b}{2}\right)p\left(\frac{a+b}{2}\right) + f(b)p(b)\right). \tag{31}$$

At the level $k = 0$ of the previous example, the evaluation of the conditional expectation $\mathbb{E}(f \mid \Xi^0)$ is obtained by means of the functional evaluation in the set $\left\{0, \frac{1}{2}, 1\right\}$. The evaluation of the conditional expectations $\mathbb{E}(f \mid \Xi_L^1)$ and $\mathbb{E}(f \mid \Xi_R^1)$ requires the functional evaluations in $\left\{0, \frac{1}{4}, \frac{1}{2}\right\}$ and $\left\{\frac{1}{2}, \frac{3}{4}, 1\right\}$ respectively. However, only the function on the set of points $\left\{\frac{1}{4}, \frac{3}{4}\right\}$ must be evaluated, because the others are already available. This makes the sequence of cell evaluations from the coarsest resolution level to the finest one, only a hierarchical representation without extra computational effort (with respect to a direct evaluation at the finest resolution level). This feature is a key aspect, when the TE framework is coupled (see Section 5) with the semi-intrusive scheme presented in Section 4. In this case, each functional evaluation is not only the evaluation of a function, but more properly a time step of the numerical scheme chosen for the discretization of the partial differential equation of interest. Moreover, not only the function should be evaluated for the quadrature, but also the numerical fluxes. These aspects are also discussed in Section 5.

DOI: 10.1002/fld

3.4. Further comments on the ENO polynomial reconstruction for the TE setting

In this section, further details on the polynomial interpolation are provided. The $\mathcal{R}_k$ operator, from a practical point of view, can be obtained by the union of all the polynomials obtained by the conservative interpolation techniques described by the equation (11). Two different operations are associated to the piecewise polynomial approximation $\mathcal{P}_j^k$. The first one is to obtain $\mathcal{P}_j^k$ from the data at the resolution level k. The second operation is the prediction of a cell average value (for a cell entirely contained in the support of the polynomial $\mathcal{P}_j^k$) at the successive resolution level (see equation (17)). The first task is to define the polynomial representation for a second order polynomial piecewise approximations ($r = 2$), over the stochastic cell Ξ_j^k:

$$\mathcal{P}_j^k = a(\xi - \xi_j^k)^2 + b(\xi - \xi_j^k) + c, \tag{32}$$

where ξ_j^k is the coordinate of the center of the stochastic cell.

To obtain the coefficients a, b and c, the conditions (11) must be fulfilled for a certain stencil. In the case of centered reconstruction, the stencil is fixed and equal to $\mathcal{S}_j = \{\Xi_{j-1}, \Xi_j, \Xi_{j+1}\}$. A linear system can be obtained as

$$\begin{cases} \mathbb{E}(\mathcal{P}_j^k \,|\, \Xi_{j-1}) = \dfrac{1}{\mu(\Xi_{j-1}^k)} \displaystyle\int_{\Xi_{j-1}^k} \mathcal{P}_j^k \mathrm{d}\xi = \left(\mathcal{D}_k f(\xi)\right)_{j-1} = v_{j-1}^k \\ \mathbb{E}(\mathcal{P}_j^k \,|\, \Xi_j) = \dfrac{1}{\mu(\Xi_j^k)} \displaystyle\int_{\Xi_j^k} \mathcal{P}_j^k \mathrm{d}\xi = \left(\mathcal{D}_k f(\xi)\right)_{j} = v_{j}^k \\ \mathbb{E}(\mathcal{P}_j^k \,|\, \Xi_{j+1}) = \dfrac{1}{\mu(\Xi_{j+1}^k)} \displaystyle\int_{\Xi_{j+1}^k} \mathcal{P}_j^k \mathrm{d}\xi = \left(\mathcal{D}_k f(\xi)\right)_{j+1} = v_{j+1}^k, \end{cases} \tag{33}$$

and for the linearity of the operator $\mathbb{E}(\bullet \,|\, \Xi)$

$$\mathbb{E}(\mathcal{P}_j^k \,|\, \Xi_j) = a\, \mathbb{E}((\xi - \xi_j^k)^2 \,|\, \Xi_j) + b\, \mathbb{E}((\xi - \xi_j^k) \,|\, \Xi_j) + c. \tag{34}$$

If the integration is performed analytically, with respect to the parameter $(\xi - \xi_j^k)$, the system becomes

$$\begin{pmatrix} \mathbb{E}((\xi - \xi_j^k)^2 \,|\, \Xi_{j-1}) & \mathbb{E}((\xi - \xi_j^k) \,|\, \Xi_{j-1}) & 1 \\ \mathbb{E}((\xi - \xi_j^k)^2 \,|\, \Xi_j) & \mathbb{E}((\xi - \xi_j^k) \,|\, \Xi_j) & 1 \\ \mathbb{E}((\xi - \xi_j^k)^2 \,|\, \Xi_{j+1}) & \mathbb{E}((\xi - \xi_j^k) \,|\, \Xi_{j+1}) & 1 \end{pmatrix} \begin{pmatrix} a \\ b \\ c \end{pmatrix} = A(\xi - \xi_j^k) \begin{pmatrix} a \\ b \\ c \end{pmatrix} = \begin{pmatrix} v_{j-1}^k \\ v_j^k \\ v_{j+1}^k \end{pmatrix}, \tag{35}$$

where the matrix $A = A(\xi - \xi_j^k)$ is dependent on the stochastic cell Ξ_j^k via its coordinate ξ_j^k. From a practical point of view, when the polynomial reconstruction should be performed over a cell Ξ_j^k, the matrix $A^{-1}(\xi - \xi_j^k)$ is first evaluated and then the vector of coefficients is obtained by the matrix vector product with the right hand side that depends on both the resolution level k and the stencil $\mathcal{S}_j$.

However, the procedure described above should be modified if the ENO interpolation is required. The only modification concerns the choice of the stencil: the procedure select the less oscillatory one between the following $\left\{\Xi_{j-2}^k, \Xi_{j-1}^k, \Xi_j^k\right\}$, $\left\{\Xi_{j-1}^k, \Xi_j^k, \Xi_{j+1}^k\right\}$ and $\left\{\Xi_j^k, \Xi_{j+1}^k, \Xi_{j+2}^k\right\}$. The smoothest one is selected choosing the one with $\min(|a|)$ following [30]. Obviously, at the boundaries of the domain, the stencil is always modified to be inside the domain. It is important to note here that the ENO reconstruction is employed along the stochastic coordinate. Thus, imposing any kind of periodicity for the cells at the boundaries in order to allow centered reconstruction is not feasible. On the contrary, reducing the stencil for the cells belonging at the boundaries introduces a reconstruction error in this cell higher than the one relative to the interior cells. This is a key aspect if a higher accuracy is desired. With the modification of the stencil, the scheme preserves its

DOI: 10.1002/fld

maximal accuracy as it is shown for the solution of the stochastic linear advection equation with smooth solution in Section 6.1.

The second task to solve is the prediction of a cell average v_j^{k+1} at the next following resolution level, if the polynomial $\mathcal{P}_j^k$ reconstruction at the previous resolution level is available (the cell $\Xi_j^{k+1} \subset \Xi_j^k$ as required by the nested character of the discretization procedure). This task is accomplished analytically in the following way. The expectation operator is applied to the polynomial $\mathcal{P}_j^k$ over the stochastic cell $\Xi_j^{k+1} \subset \Xi_j^k$

$$\mathbb{E}(\mathcal{P}_j^k \,|\, \Xi_j^{k+1}) = a\, \mathbb{E}((\xi - \xi_j^k)^2 \,|\, \Xi_j^{k+1}) + b\, \mathbb{E}((\xi - \xi_j^k) \,|\, \Xi_j^{k+1}) + c, \tag{36}$$

where the terms $\mathbb{E}((\xi - \xi_j^k)^2 \,|\, \Xi_j^{k+1})$ and $\mathbb{E}((\xi - \xi_j^k) \,|\, \Xi_j^{k+1}) + c)$ can be analytically evaluated when the cell Ξ_j^{k+1} is defined and the coefficients a, b and c are available.

The procedure described in this section is used also into the SI scheme in order to obtain the polynomial representation of the functions along the stochastic space in order to evaluate the expectation of the fluxes. The SI approach is described in the following section.

4. THE SEMI-INTRUSIVE FINITE VOLUME FORMULATION FOR PDE

In this section, the semi-intrusive (SI) approach of Abgrall and co-workers is recalled. The interested reader can refer to [7, 8] for a complete presentation of the numerical scheme and its application to different test cases. However, in the present section, the approach is presented for the first time applied to a high-resolution finite volume scheme, here the MUSCL-Hancock method, which is modified to permit an efficient and easy coupling within the TE approach presented in the previous section.

The SI method is labeled as semi-intrusive, since it requires only a limited number of modifications to an existing numerical code. In fact, the effort required is only restricted to the implementation of the specific time/spatial discretization, eventually coupled with the TE algorithm (which remains almost unchanged) to obtain the adaptive version described in this work. In particular, the SI scheme relies on the deterministic formulation available in a numerical code. Moreover, the number of equations remains equal to the original deterministic formulation, not as in the intrusive polynomial chaos method (see [5]). For that reason, the SI formulation, after the first theoretical formulation, requires only implementation modifications without any theoretical drawbacks or limitation [6]. This feature permits to obtain intrusive stochastic formulations even for high order schemes. In the present work, a second order MUSCL-Hancock method (MHM) is employed to formulate the deterministic part of the scheme; anyway the scheme is not limited to the second order of accuracy in space and in time as well, but can be extended to higher-order spatial reconstructions. This result, to the best of the author's knowledge, is the first adaptive intrusive scheme of order of spatial (and time) accuracy greater than one. Another adaptive intrusive strategy based on data-independent wavelets, limited only to first order in time and space, is the work of Tryoen et al. [12]. This work has been the first introducing wavelet adaptivity into an intrusive stochastic formulation by means of the polynomial chaos technique, but it remains very limited requiring, for each case, *ad hoc* modifications.

4.1. MUSCL-Hancock deterministic numerical formulation

The MHM is a slightly different scheme with respect to the classical predictor-corrector MUSCL one. It requires the computation of the slopes only in the predictor step. Moreover, the predictor step does not require the solution of Riemann problems. On the contrary, the corrector step is based on the evolution of cell-average quantities, taking into account the fluxes at interfaces obtained by the solutions of the corresponding Riemann problems. A generic 1D scalar conservation law is

$$\frac{\partial u(x,t)}{\partial t} + \frac{\partial f(u(x,t))}{\partial x} = 0, \tag{37}$$

DOI: 10.1002/fld

where $x \in \Omega \subset \mathbb{R}$ is the physical space and $t \in T \subset \mathbb{R}^+$ is the time space. The physical space is divided in a set of non-overlapping cells $\mathcal{C}_i$ with $\Omega = \bigcup_i \mathcal{C}_i$. The classical first order Godunov scheme, applied to (37), is obtained introducing the so-called cell-average $\bar{u}_i$ on each cell $\mathcal{C}_i$:

$$\bar{u}_i(t) = \frac{1}{|\mathcal{C}_i|} \int_{\mathcal{C}_i} u(x,t) \mathrm{d}x, \tag{38}$$

where $|\mathcal{C}_i|$ indicates the volume of the cell. Van Leer [31, 32] proposed to consider non-constant data on each cell to achieve a higher accuracy in the so-called Monotone Upstream-centered Scheme for Conservation Laws (MUSCL). The piecewise linear approximation is used for the solution $u(x,t)$ on the cell $|\mathcal{C}_i| = [x_{i_L}, x_{i_R}]$:

$$u(x,t_n) = \bar{u}_i^n + \sigma_i^n (x - x_i) \quad \text{with} \quad x_{i_L} \leq x \leq x_{i_R}, \tag{39}$$

with σ_i^n the so-called slope. Of course, the choice of $\sigma_i^n = 0$ leads to the Godunov scheme. A slope limiter should be introduced near the discontinuity to avoid oscillations. In this work, both the Roe's superbee limiter and the van Leer limiters are employed. The superbee limiter in its limited slope form is

$$\begin{cases} \sigma_i^n = \text{maxmod}\left(\sigma_{(1)}^n, \sigma_{(2)}^n\right) \\ \sigma_{(1)}^n = \text{minmod}\left(\left(\dfrac{\bar{u}_{i+1}^n - \bar{u}_i^n}{|\mathcal{C}_i|}\right), 2\left(\dfrac{\bar{u}_i^n - \bar{u}_{i-1}^n}{|\mathcal{C}_i|}\right)\right) \\ \sigma_{(2)}^n = \text{minmod}\left(2\left(\dfrac{\bar{u}_{i+1}^n - \bar{u}_i^n}{|\mathcal{C}_i|}\right), \left(\dfrac{\bar{u}_i^n - \bar{u}_{i-1}^n}{|\mathcal{C}_i|}\right)\right), \end{cases} \tag{40}$$

where the minmod and maxmod functions are defined as follows

$$\text{minmod}(a,b) = \begin{cases} a & \text{if} \quad |a| < |b| \quad \text{and} \quad ab > 0 \\ b & \text{if} \quad |a| > |b| \quad \text{and} \quad ab > 0 \\ 0 & \text{if} \quad ab \leq 0 \end{cases}$$

$$\text{maxmod}(a,b) = \begin{cases} a & \text{if} \quad |a| > |b| \quad \text{and} \quad ab > 0 \\ b & \text{if} \quad |a| < |b| \quad \text{and} \quad ab > 0 \\ 0 & \text{if} \quad ab \geq 0. \end{cases}$$

The van Leer limiter, in the form of slope limiter, is defined as (see Toro [32] for further details)

$$\sigma_i^n = \begin{cases} \text{MIN}\left(\dfrac{2R}{1+R}, \dfrac{2}{1+R}\right) \dfrac{\bar{u}_{i+1}^n - \bar{u}_{i-1}^n}{2\Delta x} & \text{if} \quad R > 0 \\ 0 & \text{if} \quad R \leq 0, \end{cases} \tag{41}$$

where R is the ratio between successive slopes $R = (\bar{u}_i^n - \bar{u}_{i-1}^n)/(\bar{u}_{i+1}^n - \bar{u}_i^n)$.

The MHM is then introduced in order to avoid the problem related to the solution of the so-called generalized Riemann problem, in which the two states are not constant. The fully discrete second order MHM, written for computing each cell-average value $\bar{u}_i^{n+1}$ separately, consists of the following three steps:

- Step 1 - For each cell $\mathcal{C}_\ell \in \{\mathcal{C}_{i-1}, \mathcal{C}_i, \mathcal{C}_{i+1}\}$, the solution at the interface is computed according to

$$\begin{cases} u_{\ell_L}^n = \bar{u}_\ell^n - \sigma_\ell^n \dfrac{|\mathcal{C}_\ell|}{2} \\ u_{\ell_R}^n = \bar{u}_\ell^n + \sigma_\ell^n \dfrac{|\mathcal{C}_\ell|}{2} \end{cases} \tag{42}$$

DOI: 10.1002/fld

- Step 2 - On each cell $\mathcal{C}_\ell \in \{\mathcal{C}_{i-1}, \mathcal{C}_i, \mathcal{C}_{i+1}\}$, the extrapolated values evolve of a half time step employing the flux function $f = f(u)$ (without requiring the solution of Riemann problems):

$$\begin{cases} u^{\Uparrow}_{\ell_R} = u^n_{\ell_R} + \dfrac{1}{2}\dfrac{\Delta t}{|\mathcal{C}_\ell|}\left(f(u^n_{\ell_L}) - f(u^n_{\ell_R})\right) \\ u^{\Uparrow}_{\ell_L} = u^n_{\ell_L} + \dfrac{1}{2}\dfrac{\Delta t}{|\mathcal{C}_\ell|}\left(f(u^n_{\ell_L}) - f(u^n_{\ell_R})\right) \end{cases} \tag{43}$$

- Step 3 - The cell-average value on the cell $\mathcal{C}_i$ evolves following

$$\bar{u}^{n+1}_i = \bar{u}^n_i - \frac{\Delta t}{|\mathcal{C}_i|}\left(\mathcal{F}^{\mathrm{RM}}\left(u^{\Uparrow}_{i-1_R}, u^{\Uparrow}_{i_L}\right) - \mathcal{F}^{\mathrm{RM}}\left(u^{\Uparrow}_{i_R}, u^{\Uparrow}_{i+1_L}\right)\right). \tag{44}$$

The symbol $\mathcal{F}^{\mathrm{RM}}$ is employed to indicate the flux evaluated at the interface, after the solution of the Riemann problem defined by two constant states based on the evolved extrapolated values. For the linear advection, in Section 6.1, and Burgers equation, in Section 6.2, an exact Riemann solver is used. Moreover, in the case of the Euler system of equations, in Section 6.3, the Roe-Pike method is employed with the Harten-Hyman entropy fix following [32].

As it is evident, the time advancing formula is limited to a stencil of only three cells $\mathcal{C}_{i-1}$, $\mathcal{C}_i$ and $\mathcal{C}_{i+1}$. However, the computation of the slopes for the cells $\mathcal{C}_{i-1}$ and $\mathcal{C}_{i+1}$ requires (see (40) and (41)) also to know the solutions on the two surrounding cells $\mathcal{C}_{i-2}$ and $\mathcal{C}_{i+2}$. The average solution $\bar{u}^{n+1}_i$, on each cell $\mathcal{C}_i$ at time $t_{n+1} = t_n + \Delta t$, can be computed knowing the solution on the augmented stencil $\left\{\bar{u}^n_{i-2}, \bar{u}^n_{i-1}, \bar{u}^n_i, \bar{u}^n_{i+1}, \bar{u}^n_{i+2}\right\}$, referred in the following as the Physical Vector (PV).

4.2. Semi-intrusive formulation for the MHM

The SI version of the MHM (here presented in the 1D stochastic case without loss of generality) can be obtained adding one dimension more (the stochastic space) with a finite-volume like representation. In particular, the conditional expectation operator, defined on the stochastic cell Ξ_j, is introduced according to the following definition:

$$\mathbb{E}(\bullet \,|\, \Xi_j) = \frac{1}{\mu(\Xi_j)} \int_{\Xi_j} \bullet(x, \xi, t)\, p(\xi, t)\, \mathrm{d}\xi. \tag{45}$$

If the conditional expectation operator is applied to the Step 3 of the MHM scheme (44), the following scheme is obtained:

$$\mathbb{E}(u^{n+1}_i \,|\, \Xi_j) = \mathbb{E}(u^n_i \,|\, \Xi_j) - \frac{\Delta t}{|\mathcal{C}_i|}\left(\mathbb{E}(\mathcal{F}^{\mathrm{RM}}\left(u^{\Uparrow}_{i-1_R}, u^{\Uparrow}_{i_L}\right) \,|\, \Xi_j) - \mathbb{E}(\mathcal{F}^{\mathrm{RM}}\left(u^{\Uparrow}_{i_R}, u^{\Uparrow}_{i+1_L}\right) \,|\, \Xi_j)\right). \tag{46}$$

The evaluation of the updated conditional expected value on the cell Ξ_j, is obtained by evaluating the expectation of the contributions related to the numerical fluxes $\mathbb{E}(\mathcal{F}^{\mathrm{RM}}\left(u^{\Uparrow}_{i-1_R}, u^{\Uparrow}_{i_L}\right) \,|\, \Xi_j)$ and $\mathbb{E}(\mathcal{F}^{\mathrm{RM}}\left(u^{\Uparrow}_{i_R}, u^{\Uparrow}_{i+1_L}\right) \,|\, \Xi_j)$. Evaluating these integral contributions requires to know the polynomial representation of the physical averaged solution over the whole stochastic dimensions. The conservative interpolation procedure, already presented in Section 3 to obtain the reconstruction operator $\mathcal{R}_k$, can be adopted requiring for the polynomial $\mathcal{P}_j(\xi)$:

$$\mathbb{E}(P_\ell(\xi) \,|\, \Xi_\ell) = \mathbb{E}(u \,|\, \Xi_\ell) \quad \forall \Xi_\ell \in \mathcal{S}_j \tag{47}$$

If the stencil $\mathcal{S}_j$ is chosen with a cardinality $s = s(r) = \mathrm{card}(\mathcal{S}_j) = r + 1$ (for a 1D space), a polynomial $\mathcal{P}_j(\xi)$ of degree r can be built.

The polynomial representation $\mathcal{P}_j(\xi)$ can be injected into the Step 1 (42) and Step 2 (43) of the MHM. If the Cavalieri-Simpson rule (using three quadrature points $ng = 3$) is adopted for the quadrature, the SI scheme for the MHM can be written in a form which makes easy the use of the TE strategy for the representation of the stochastic data.

DOI: 10.1002/fld

It is assumed a uniform tessellation for the physical and stochastic space, with a number of cells equal to N_x and N_ξ respectively, and a constant time step Δt. The first step is to evaluate the initial condition in terms of conditional expectations. This can be obtained easily via a tensorization of the quadrature rule and evaluating the analytical value of the function $u(x,\xi,0)$. This step yields the stochastic initial condition $\mathbb{E}(u_i(x,\xi,0)\,|\,\Xi_j)$ for all $i=1,\dots,N_x$ and $j=1,\dots,N_\xi$.

The global SI algorithm can be resumed as follows:

Algorithm 3: Semi-intrusive version of the MUSCL-Hancock method for a 1D stochastic space.

for $n=1,\dots,N_t$ **do**
  for $i=1,\dots,N_x$ **do**
    for $j=1,\dots,N_\xi$ **do**
      $\forall \bar{u}_\ell^n(\xi)\in \mathrm{PV}$
      Polynomial reconstruction (via (47)) over $\Xi_j=[\xi_{j-1},\xi_j]\Rightarrow \mathcal{P}_j(\xi)$
      for $ng=1,\dots,3$ **do**
        $\xi_{ng}=\xi_{j-1}+\frac{\xi_j-\xi_{j-1}}{2}(ng-1)$
        Evaluation of $\mathrm{PV}(\xi_{ng})$
        Slope computation (and limiting)
        Step 1 (see (42)) $\Rightarrow \forall \mathcal{C}_\ell\in\{\mathcal{C}_{i-1},\mathcal{C}_i,\mathcal{C}_{i+1},\}\rightarrow\left\{u^n_{\ell_L}(\xi_{ng}),u^n_{\ell_R}(\xi_{ng})\right\}$
        Step 2 (see (43)) $\Rightarrow \forall \mathcal{C}_\ell\in\{\mathcal{C}_{i-1},\mathcal{C}_i,\mathcal{C}_{i+1},\}\rightarrow\left\{u^{\Uparrow}_{\ell_L}(\xi_{ng}),u^{\Uparrow}_{\ell_R}(\xi_{ng})\right\}$
      end
      Flux expectations computation:
      $\mathbb{E}(\mathcal{F}_L^{\mathrm{RM}}\,|\,\Xi_j)=\sum_{ng=1}^3 w_{ng}\,\mathcal{F}^{\mathrm{RM}}\left(u^{\Uparrow}_{i-1_R}(\xi_{ng}),u^{\Uparrow}_{i_L}(\xi_{ng}),\xi_{ng}\right)$;
      $\mathbb{E}(\mathcal{F}_R^{\mathrm{RM}}\,|\,\Xi_j)=\sum_{ng=1}^3 w_{ng}\,\mathcal{F}^{\mathrm{RM}}\left(u^{\Uparrow}_{i_R}(\xi_{ng}),u^{\Uparrow}_{i+1_L}(\xi_{ng}),\xi_{ng}\right)$;
      Time update:
      $\mathbb{E}(\bar{u}_i^{n+1}\,|\,\Xi_j)=\mathbb{E}(\bar{u}_i^{n}\,|\,\Xi_j)-\frac{\Delta t}{|\mathcal{C}_i|}\left(\mathbb{E}(\mathcal{F}_L^{\mathrm{RM}}\,|\,\Xi_j)-\mathbb{E}(\mathcal{F}_R^{\mathrm{RM}}\,|\,\Xi_j)\right)$
    end
  end
end

5. THE OVERALL MULTIRESOLUTION ADAPTIVE-SI SCHEME

The adaptive version of the numerical algorithm (aSI) is described in this section. Note that the present paper deals with 1D problems in both the physical and stochastic space even if the algorithm presented are completely general. However, in Section 5.1, some remarks on the multidimensional extension are discussed.

Main difference, referring to the algorithm 3 is in the internal loop, on j, concerning the stochastic cells. This loop should be replaced with the application of the TE algorithm 1. The discretization step is performed by the application of the MHM, as presented in the internal loop (on j), in the

DOI: 10.1002/fld

algorithm 3. The complete aSI scheme is as follows:

Algorithm 4: Semi-intrusive version of the MUSCL-Hancock method for a 1D stochastic space.

for $n = 1, \dots, N_t$ **do**
  for $i = 1, \dots, N_x$ **do**
    while $2 \leq k \leq L$ **do**
      for $j = 1, \dots, J_{k-2}$ **do**
        Encoding:
        $d_j^{k-1} = v_{2j}^{k-1} - (\mathrm{P}_{k-2}^{k-1} v^{k-2})_{2j} = v_{2j}^{k-1} - \left(\frac{1}{\mu(\Xi_{2j}^{k-1})} \int_{\Xi_{2j}^{k-1}} \mathcal{R}_{k-2} v^{k-2} p(\xi) \mathrm{d}\xi \right)$;
        Truncation: $\hat{d}_j^{k-1} = \mathrm{tr}(d_j^{k-1}, \varepsilon_{k-1})$;
      end
      Level Advancement: $(\mathcal{G}^{k-1}, \hat{d}^{k-1}) \to \mathcal{G}^k$
      for $j = 1, \dots, J_{k-1}$ **do**
        if $\hat{d}_j^{k-1} > 0$ **then**
          Discretization:
          for $\Xi_q \in \left\{ \Xi_{2j-1}^k, \Xi_{2j}^k \right\}$ **do**
            for $ng = 1, \dots, 3$ **do**
              $\forall \bar{u}_\ell^n(\xi) \in \mathrm{PV}(\xi)$
              Polynomial evaluation: $\bar{u}_\ell^n(\xi_{ng}) \simeq (\mathcal{R}_L v^L(t_n))(\xi_{ng})$
              Slope computation (and limiting)
              Step 1 (see (42))
              $\Rightarrow \forall \mathcal{C}_\ell \in \{\mathcal{C}_{i-1}, \mathcal{C}_i, \mathcal{C}_{i+1}, \} \to \left\{ u_{\ell_L}^n(\xi_{ng}), u_{\ell_R}^n(\xi_{ng}) \right\}$
              Step 2 (see (43))
              $\Rightarrow \forall \mathcal{C}_\ell \in \{\mathcal{C}_{i-1}, \mathcal{C}_i, \mathcal{C}_{i+1}, \} \to \left\{ u_{\ell_L}^{\Uparrow}(\xi_{ng}), u_{\ell_R}^{\Uparrow}(\xi_{ng}) \right\}$
            end
            Flux expectations computation:
            $\mathbb{E}(\mathcal{F}_L^{\mathrm{RM}} \,|\, \Xi_q) = \sum_{ng=1}^3 w_{ng} \, \mathcal{F}^{\mathrm{RM}} \left(u_{i-1_R}^{\Uparrow}(\xi_{ng}), u_{i_L}^{\Uparrow}(\xi_{ng}), \xi_{ng} \right)$
            $\mathbb{E}(\mathcal{F}_R^{\mathrm{RM}} \,|\, \Xi_q) = \sum_{ng=1}^3 w_{ng} \, \mathcal{F}^{\mathrm{RM}} \left(u_{i_R}^{\Uparrow}(\xi_{ng}), u_{i+1_L}^{\Uparrow}(\xi_{ng}), \xi_{ng} \right)$
            Cell agglomeration of $\mathbb{E}(u_i^n \,|\, \Xi_q)$ via equation (49)
            Time update:
            $\mathbb{E}(\bar{u}_i^{n+1} \,|\, \Xi_q) = \mathbb{E}(\bar{u}_i^n \,|\, \Xi_q) - \frac{\Delta t}{|\mathcal{C}_i|} \left(\mathbb{E}(\mathcal{F}_L^{\mathrm{RM}} \,|\, \Xi_q) - \mathbb{E}(\mathcal{F}_R^{\mathrm{RM}} \,|\, \Xi_q) \right)$
          end
        end
      end
    end
    Reconstruction: $(\mathcal{D}_L \mathcal{R}_L v^L)_l = (\mathcal{D}_L \bar{u}(x_i, \xi, t_{n+1}))_l \quad \text{with} \quad l \in \mathcal{S}_j^L$;
  end
end

One of the main links between the SI and the TE strategy is constituted by the polynomial reconstruction. The SI scheme requires the polynomial reconstruction over each stochastic cell; if on each cell the conservative reconstruction (see Section 3.4) is adopted to obtain $\mathcal{P}_j$, their union is exactly the reconstruction operator $\mathcal{R}_k$ (fixing the physical coordinate). The polynomial reconstruction can be performed when the finest resolution $k = L$ is reached for each physical and time coordinate; its value is thus stored to be available at the following time step. The reconstruction operator is used for the polynomial evaluation, before computing the slopes and applying the Step 1. Moreover, a conservative interpolation is also present into the TE algorithm, where the

DOI: 10.1002/fld

operator $\mathcal{R}_k$ is used to obtain the wavelets during the *encoding* procedure. In this case, however, the reconstruction operator cannot be obtained by the one relative to the previous time step, but is evaluated at the current time step.

The modification of the tessellation with the time and, consequently the data-representation, is another important feature, of the aSI algorithm, which is totally absent in the baseline SI scheme. This feature is fundamental for locally refining/coarsening the stochastic space, as a function of the variation of the solution regularity during the computation. At the end of each time step, for each physical location, the algorithm produces a sequence of conditional expected values $\mathbb{E}(u^n \,|\, \Xi_j)$ with different measures $\mu(\Xi_j)$, due to the local refinement/coarsening of the tessellation (consequently, on each cell the solution is represented by means of a different polynomial). The TE strategy starts from the coarsest level to the finest (until some cells should be divided or the maximum resolution level is reached). In practice, if a cell is not divided, it is moved at the highest resolution level. The *Level Advancement* strategy is performed as it has been described in Section 3.2.

The local variation of the stochastic tessellation, depending on the physical and time coordinates, implies solving two different issues. The TE strategy is performed at the time step $n+1$, when all the quantities are known at time n. While the algorithm proceeds towards the finest resolution level, also the tessellation at time $n+1$ is obtained. The *Level Advancement* strategy must be intended at time $n+1$, since based on discrete values which are the conditional expected values at time $n+1$. For this reason, the time update procedure, formally analogous to the classical finite volume in the deterministic case, results to be slightly different. The time update step can be written as follows, making explicit the dependence on the time coordinates and on the resolution level for the tessellation, for a generic cell $\Xi_j^{k,n+1}$, i.e. a cell belonging to a resolution level k defined at the time step $n+1$

$$\mathbb{E}(\bar{u}_i^{n+1} \,|\, \Xi_j^{k,n+1}) = \mathbb{E}(\bar{u}_i^{n} \,|\, \Xi_j^{k,n+1}) - \frac{\Delta t}{|\mathcal{C}_i|}\left(\mathbb{E}(\mathcal{F}_L^{\mathrm{RM}} \,|\, \Xi_j^{k,n+1}) - \mathbb{E}(\mathcal{F}_R^{\mathrm{RM}} \,|\, \Xi_j^{k,n+1})\right). \tag{48}$$

Note that the conditional expected value at time n, $\mathbb{E}(\bar{u}_i^n \,|\, \Xi_j^{k,n+1})$, the first term at the right hands side, should be evaluated on the cell $\Xi_j^{k,n+1}$, obtained by dividing its mother cell at the previous resolution level but at the current time step $n+1$. This cell could not exist at time n. Thus, two different cases are possible: the actual resolution level, *i.e.* at time $n+1$, can be either higher or lower than the resolution level at the previous time step n. In the first case, the quantities can be obtained by applying the discretization operator, on the cell of interest at time $n+1$, to the reconstruction operator obtained for quantities at time n. This is possible because the tessellations, even if time dependent, are always nested. The second case is relative to an actual $(n+1)$ resolution level, which is lower than the one at the previous time step. In this case, the conditional expected value should be obtained by the agglomeration of all the stochastic cells belonging to it. Following the exact definition, it is possible to write

$$\mathbb{E}(\bar{u}_i^n \,|\, \Xi_j^{k,n+1}) = \frac{1}{\mu(\Xi_j^{k,n+1})} \sum_{\Xi_\ell^{L,n} \subseteq \Xi_j^{k,n+1}} \mu(\Xi_\ell^{L,n}) \mathbb{E}(\bar{u}_i^n \,|\, \Xi_\ell^{L,n}). \tag{49}$$

Obviously, it is easy to verify that the limit case is the one with a cell not subdivided, then the equation (49) reduces to an identity. Due to the nested sequences of operators and meshes, a cell would always be constituted by an integer number of cells at the end of the TE algorithm (see algorithm 1).

For resuming, the value of $\mathbb{E}(\bar{u}_i^n \,|\, \Xi_j^{k,n+1})$ can be computed as

$$\mathbb{E}(\bar{u}_i^n \,|\, \Xi_{j_{n+1}}^{k,n+1}) = \begin{cases} \dfrac{1}{\mu(\Xi_j^{k,n+1})} \displaystyle\sum_{l=1}^{\bar{l}} \mu(\Xi_l^{L,n})\, \mathbb{E}(\bar{u}_i^n \,|\, \Xi_l^{L,n}) & \text{if} \quad \Xi_j^{k,n+1} = \displaystyle\bigcup_{l=1}^{\bar{l}} \Xi_l^{L,n} \\ \dfrac{1}{\mu(\Xi_j^{k,n+1})} \displaystyle\int_{\Xi_j^{k,n+1}} \mathcal{R}_{L,n} v^{L,n} \mathrm{d}\mu & \text{otherwise} \end{cases} \tag{50}$$

DOI: 10.1002/fld

Another issue concerns the possibility to introduce the adaptation strategy by preserving the computational efficiency.

This is related to reduce the computational cost basing on the computed quantities, when a cell has to be splitted. For this reason, the quadrature rule of Newton-Cotes is adopted. In this case, the entire set of degrees of freedom (dof) can be saved, if the cell has to be split. Let us consider the figure 3, where the Cavalieri-Simpson rule is used. On the left, the cell at level k is represented with its dof, the circles are used for the value of $\bar{u}_i$ obtained via the polynomial $\mathcal{P}_j$ (the polynomial evaluation step in the algorithm 4), and squares for the fluxes obtained after the application of the step 1 and 2 of the MHM. When the cell is split in two cells, only three points have to be added (the numerical scheme should be applied). On the contrary, the other points can be obtained directly from the mother cell at level k. In figure 3, the black circle/squares represent the new points to compute. In practice, the black points are associated to the values for $\bar{u}_i$ obtained by interpolation and the fluxes are obtained via the Step 1 and 2; otherwise, they are only recovered from the mother cell. Finally, the fluxes conditional expectation computation is performed easily by combining the new fluxes (black) and the old ones (white) with the correct weights for the quadrature.

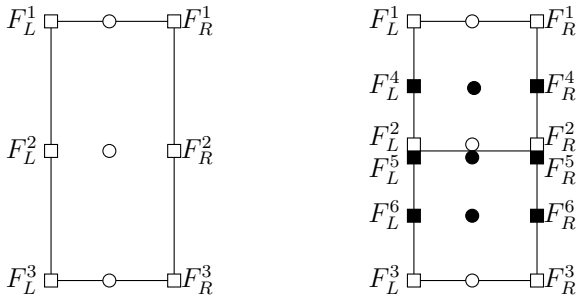

Figure 3. Example of a splitting procedure to save the computational cost associated to the degree of freedom already computed. On the left, the cell at level of resolution k is reported while on the right the corresponding split cells are reported with the new points to explicitly add (black symbols).

The nested procedure described above allows to extend the accuracy of the quadrature rule even to high-order Newton-Cotes formula. Moreover, in the present work, the three points Cavalieri-Simpson rule (see (31)) is employed. The error is proportional to the fourth derivative of the integrand, so the rule is fully accurate for a polynomial function of order equal or less than three (see [29] for further details). In the following, the variance of the outputs of interest is computed. In this case, the quadrature of the polynomial $\mathcal{P}_j$ squared has to be evaluated on each cell $\Xi_j = [\xi_a, \xi_b]$. In order to attain the exact integration of $\mathcal{P}_j^2$, the closed four points Newton-Cotes rule (also known as the Boole's rule) is employed

$$\int_{\Xi_j} f(\xi)\mathrm{d}\xi = \frac{\xi_b - \xi_a}{90}\left(7f(\xi_a) + 32f\left(\xi_a + \frac{\xi_b - \xi_a}{4}\right) + 12f\left(\xi_a + \frac{\xi_b - \xi_a}{2}\right) + 32f\left(\xi_a + 3\frac{\xi_b - \xi_a}{4}\right) + 7f(\xi_b)\right). \tag{51}$$

The last five points rule has an error $\mathcal{O}(f^{(6)}(\eta))$, where $\eta \in]\xi_a, \xi_b[$, so it is able to integrate exactly polynomial function of order equal to five.

5.1. Multidimensional extension

In this section, some comments on the multidimensional extension of the aSI scheme are provided. However, the application of the aSI scheme in dimension greater than one is beyond the scope of the present paper. First of all, it is necessary to clarify what is intended here for multidimensional algorithm. If a spatial domain $\Omega \subset \mathbb{R}^{n_d}$, with $n_d = 2, 3$, is of interest, the aSI scheme described by

DOI: 10.1002/fld

the Algorithm 4 can be extended in a straightforward manner, by considering just the number of spatial cell N_x as the total number of spatial cell in the domain.

Then, the focus is devoted to the extension of the dimension of the stochastic space $\Xi \subset \mathbb{R}^d$, with $d > 1$. For simplicity, it is possible to identify two classes of modifications: the ones which are related to the TE algorithm itself, and the other involving deeply the SI scheme. The main modification to the TE algorithm are relative to the generation of a tessellation in many dimensions, potentially more than three. Despite the generality of the TE framework, which can be applied on any kind of meshes, even non-uniform and unstructured (see for instance the classical MR counterpart in [25]), in the context of stochastic partial differential equations, it is likely to refer to stochastic space which are hypercubes (of course if it is assumed that the stochastic variables are independent). The generation of the meshes can be handled, in principle, in a Cartesian setting. Then, each cell can be subdivided in 2^d sub-cells. Obviously, this strategy could be not very effective, when high-gradients are located in narrow regions. However, the general flexibility of the algorithm allows the use of non-uniform tessellations and a cell can be still divided in two sub-cell obtaining an anisotropy mesh refinement. All the basics tools presented in Section 3.1 remains valid until the relation (14) holds; this can be accomplished without any limitation on the refinement (cell by cell). The other point which requires some attention, concerning the TE algorithm, is the polynomial reconstruction. Many papers exists in literature, which are devoted to the theoretical and numerical implementation of different strategies. For instance, the interested reader can refer to [30, 27] for the ENO reconstruction problem. The major issues derive from the choice of a non-linear reconstruction operator and of the stencil. The polynomial reconstruction step is related also to the relation between the TE algorithm and the SI approach. As described in the previous sections, the polynomial reconstruction is employed to evaluate the expectations of the numerical fluxes. Moreover, another ingredient of the aSI scheme is the quadrature technique to employ for the evaluations of the conditional expectations. In Section 3.3, for instance, it has been described how the Newton-Cotes quadrature rule can be employed. The tensorization of this 1D quadrature rules is still nested and symmetric, thus it is capable to preserve the efficiency of the scheme. Indeed, even if the aSI scheme is efficient in the reduction of the active cells in which the solution should be explicitly computed, it appears clear that a technique to reduce the numerical cost of a quadrature rule in many dimensions could contribute to reduce more the overall cost of the algorithm. For instance, the link between the Newton-Cotes and the sparse grids is reported in [33]. To summarize, the theoretical tools needed for the multidimensional extension of both the TE and aSI algorithm are already available, while most of the effort should be devoted to the implementation of the strategies described above. Moreover, the aSI algorithm in the form reported in the Algorithm 4 can be easily massively parallelized because any spatial coordinate is independent by the others and the TE loop can be accomplished employing only information at the previous time step.

6. NUMERICAL RESULTS

In this section, several results are presented. The aim is to show the convergence properties of aSI scheme and to provide some evidences of the advantage to employ an adaptive representation of the solution in the stochastic space. For all the problems, the expectation and the variance of the outputs are computed according to the definitions (2) with respect to the exact value. Different 1D-1D test cases are taken into account. The linear advection problem is solved for both smooth and discontinuous initial conditions in Section 6.1. In the first case, the uncertainty is considered in the initial condition, while in the discontinuous case an uncertain advection velocity is considered. For this test case, both the convergence curves for the first order Godunov method and the MHM are reported to demonstrate the ability of the scheme to maintain the convergence properties of the deterministic scheme. The Burgers equation is then solved by employing a smooth initial, but uncertain, initial condition in Section 6.2. This case is chosen in order to demonstrate the ability of the scheme to capture (refining the stochastic space) a discontinuous solution even if the discontinuities form during the evolution of a smooth solution. This property is a key feature in the development of numerical schemes for UQ in compressible flows applications. The last test-case is

DOI: 10.1002/fld

the stochastic analysis of the uncertain shock tube problem in Section 6.3. In this case, the statistics of the density are compared to the semi-analytical solution of the Euler equations, considering an uncertain parameter on the initial conditions (see Appendix .1).

Systematically, in this paper, the spatial norms are computed by employing the following definitions

$$\begin{cases} \mathrm{err}_{\mathcal{E}^m}|_{L^p} = ||\mathcal{E}^m(x) - \mathcal{E}^m_{\mathrm{ref}}(x)||_{L^p} = \left(\dfrac{1}{N_x} \displaystyle\sum_{i=1}^{N_x} |\mathcal{E}^m(\bar{u}_i) - \mathcal{E}^m_{\mathrm{ref}}(\bar{u}_i)|^p \right)^{1/p} \\ \mathrm{err}_{\mathcal{E}^m}|_{L^\infty} = ||\mathcal{E}^m(x) - \mathcal{E}^m_{\mathrm{ref}}(x)||_{L^\infty} = \max\limits_i |\mathcal{E}^m(\bar{u}_i) - \mathcal{E}^m_{\mathrm{ref}}(\bar{u}_i)| \,, \end{cases} \tag{52}$$

where the integer $p = 1, 2$ for the L^1 and L^2 norms in the physical space and $\mathcal{E}^m$ indicates a statistical moment, *i.e.* the expectation or the variance.

6.1. *Linear advection*

The first test-case is the linear advection problem in the general stochastic formulation

$$\begin{cases} \dfrac{\partial u(x,\xi,t)}{\partial t} + a(\xi)\dfrac{\partial u(x,\xi,t)}{\partial x} = 0 \\ u(x,\xi,0) = u_0(x,\xi), \end{cases} \tag{53}$$

where both the advection velocity a and the initial condition u_0 can depend on a random parameter and $\Omega = [0, 1]$.

Let us consider first the smooth test-case with an initial condition equal to $u_0(x, \xi, t) = sin(4\pi x + 20\xi)$, with the random parameter uniformly distributed $\xi \sim \mathcal{U}[0, 1]$. The problem is solved until the time $t = 1$ with a constant advection velocity equal to $a = 0.1$ and with periodic boundary conditions. The exact solution can be computed analytically as follows

$$u(x, \xi, 1) = sin(4(x - 0.1t)\pi + 20\xi). \tag{54}$$

The exact statistics can be computed as a function of the ith cell $\mathcal{C}_i = [x_i - \frac{|\mathcal{C}_i|}{2}, x_i + \frac{|\mathcal{C}_i|}{2}]$, for $\mathcal{C}_i \to 0$:

$$\begin{cases} \mathcal{E}(\bar{u}_i) = \displaystyle\int_\Xi u(x_i, \xi, 1)\, \mathrm{d}\xi \\ \mathrm{Var}(\bar{u}_i) = \displaystyle\int_\Xi u^2(x_i, \xi, 1)\, \mathrm{d}\xi - \left(\int_\Xi u^2(x_i, \xi, 1)\, \mathrm{d}\xi \right)^2 . \end{cases} \tag{55}$$

Expressions for both statistics are obtained using the MAPLE software. Numerical simulations are carried out on equally spaced spatial meshes of 51, 101, 201 and 401 points, with $N_t = 200$ time steps and $\Delta t = 5 \times 10^{-3}$.

In figure 4, both the expectation of the solution 4(a) and the variance 4(a) for the linear advection problem (53) with smooth initial condition and constant advection velocity are reported. The continuous lines indicate the solution obtained via the scheme without compression, while the dashed lines indicate the solution obtained via the application of the aSI algorithm. In particular, the polynomial reconstruction is taken as a centered second-order polynomial except for the two boundary cells where the stencil is fully shifted into the numerical domain in order to preserve the order of accuracy. In particular, both the Godunov first order scheme and the MHM are reported to show that the numerical scheme is able to preserve the expected order of convergence even in presence of adaptivity and with compression. To preserve the formal second order of accuracy, the slope for the MHM is evaluated by a centered approximation without any limiter function. The full solution is obtained on an equally spaced mesh of 128 stochastic cells, while the aSI algorithm is applied by starting from a coarse level of 16 cell ($m_0 = 4$) to a higher resolution level of 128 cells ($m = 7$) and a threshold equal to $\varepsilon = 10^{-3}$. Note that the finest level is indicated as m. This case is reported in order to show the formal accuracy of the method, because the solution is regular enough

DOI: 10.1002/fld

to minimize the gain associated to the compression of the solution. In particular, the average number of cells employed by the aSI scheme is 126 against the 128 of the full solution. Of course, the level of compression could be easily increased in this case by employing a higher order polynomial $\mathcal{P}_j$ for the reconstruction. Remark that, concerning the accuracy, the stochastic reconstruction (quadratic polynomial) is sufficiently accurate with respect to the spatial and time accuracy (second order in the case of MHM). On the contrary, concerning the compression, a higher polynomial order can yield a stronger compression keeping the second order convergence rate. As evident from the figures 4(a), the lines (aSI and full) are almost indistinguishable; this means that the adaptivity does not alter the overall accuracy of the scheme.

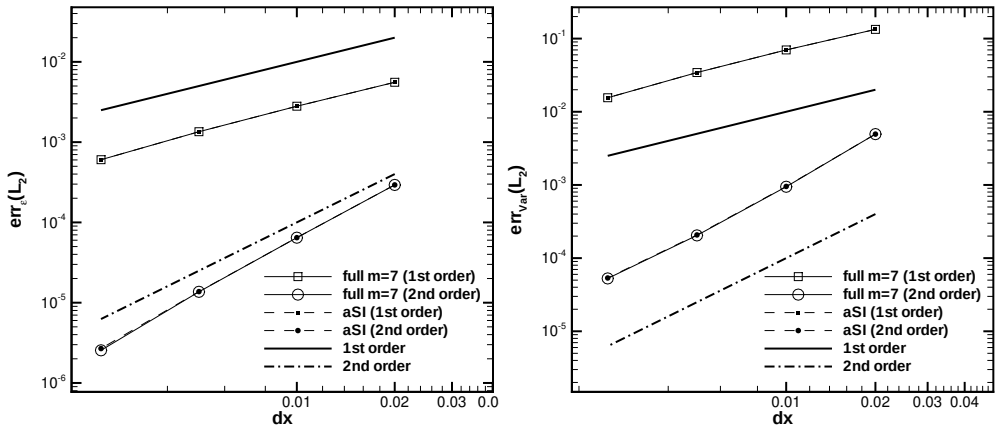

(a) (b)

Figure 4. Spatial convergence for the linear advection problem with smooth initial condition (54). The statistics of the solution (mean (a) and variance (b)) obtained with (aSI) and without (full) compression are reported for both the Godunov first order scheme and the MHM method with a centered slope.

The second test case is the linear advection problem (53), which is solved with an uncertain advection ($\xi \sim \mathcal{U}[\frac{1}{5}, \frac{4}{5}]$) velocity defined as

$$a(\xi) = \frac{1}{40} e^{5\xi^2} + \frac{1}{5}, \tag{56}$$

considering a discontinuous initial condition (in the physical space)

$$u(x, \xi, 0) = \begin{cases} 1 & \text{if} \quad \dfrac{2}{5} \leq x \leq \dfrac{3}{5} \\ 0 & \text{if} \quad \text{otherwise.} \end{cases} \tag{57}$$

In this case, the problem is solved until the final time of $t = 0.4$ with 200 equal steps of $\Delta t = 2 \times 10^{-3}$. The exact solution is derived, for the first two statistical moments, by employing the following procedure. Referring to the figure 5, starting from the initial condition (defined by the points A_1, A_2, B_2, B_1), the new points (coordinates in the physical space) at the final time ($t = 0.4$)

DOI: 10.1002/fld

can be computed as follows

$$\begin{cases} A_1^{\prime,x} = A_1^x + a\left(\frac{1}{5}\right)t = \frac{12}{25} + \frac{1}{100}e^{\frac{1}{5}} \\ A_2^{\prime,x} = A_2^x + a\left(\frac{1}{5}\right)t = \frac{12}{25} + \frac{1}{100}e^{\frac{1}{5}} \\ B_1^{\prime,x} = B_1^x + a\left(\frac{1}{5}\right)t = \frac{12}{25} + \frac{1}{100}e^{\frac{16}{25}} \\ B_2^{\prime,x} = B_2^x + a\left(\frac{1}{5}\right)t = \frac{12}{25} + \frac{1}{100}e^{\frac{16}{25}}. \end{cases} \tag{58}$$

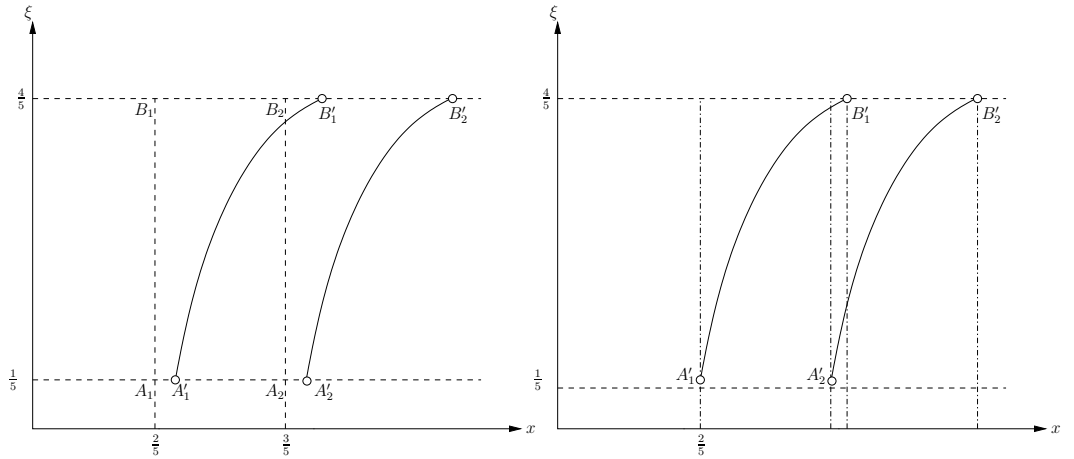

Figure 5. Schematic representation of the evolution between the initial condition (points A_1, A_2, B_1, B_2) and the final condition at time $t = 0.4$ (points A'_1, A'_2, B'_1, B'_2) (a). The regions where the exact solution should be computed, at the final time $t = 0.4$, are reported in (b).

At the final time step, four different regions can be identified (see figure 5(b)). The solution in the external region, where $x \leq A_1^{\prime,x}$ and $x \geq B_2^{\prime,x}$, is easily identified as $u(x, \xi, t) = 0$. For the remaining regions, the position of the discontinuity should be computed. In particular, it is possible to define the two functions $\xi_d^1 = \xi_d^1(x)$ and $\xi_d^2 = \xi_d^2(x)$ as the positions of the discontinuities for each x belonging respectively to the intervals $[A_1^{\prime,x}, B_1^{\prime,x}]$ and $[A_2^{\prime,x}, B_2^{\prime,x}]$. If x belongs to the interval defined above, the following relations must hold

$$\begin{cases} x = A_1^{\prime,x} + a\left(\xi_d^1\right)t = \frac{12}{25} + \frac{1}{100}e^{(\xi_d^1)^2} & \text{if} \quad x \in [A_1^{\prime,x}, B_1^{\prime,x}] \\ x = A_2^{\prime,x} + a\left(\xi_d^2\right)t = \frac{17}{25} + \frac{1}{100}e^{(\xi_d^2)^2} & \text{if} \quad x \in [A_2^{\prime,x}, B_2^{\prime,x}]. \end{cases} \tag{59}$$

As a consequence, the position of the discontinuities, for a certain physical position can be derived

$$\begin{cases} \xi_d^1 = \xi_d^1(x) = \sqrt{\ln\left(100\left(x - \frac{12}{25}\right)\right)} \\ \xi_d^2 = \xi_d^2(x) = \sqrt{\ln\left(100\left(x - \frac{17}{25}\right)\right)}. \end{cases} \tag{60}$$

DOI: 10.1002/fld

The exact statistics of the physical cell average $\bar{u}_i$ can be computed exactly for each cell $\mathcal{C}_i = \left[x_i - \frac{|\mathcal{C}_i|}{2}, x_i + \frac{|\mathcal{C}_i|}{2}\right]$ (in the limit of $|\mathcal{C}_i| \to 0$). For the mean, they are defined as

$$\mathcal{E}(\bar{u}_i) = \begin{cases} 0 & \text{if} \quad x_i \leq A_1'^{,x} \text{ or } x_i \geq B_2'^{,x} \\ \frac{5}{3}\left(\xi_d^1(x_i) - \frac{1}{5}\right) & \text{if} \quad x_i \in [A_1'^{,x}, A_2'^{,x}] \\ \frac{5}{3}\left(\xi_d^1(x_i) - \xi_d^2(x_i)\right) & \text{if} \quad x_i \in [A_2'^{,x}, B_1'^{,x}] \\ \frac{5}{3}\left(\frac{4}{5} - \xi_d^2(x_i)\right) & \text{if} \quad x_i \in [B_1'^{,x}, B_2'^{,x}]. \end{cases} \tag{61}$$

Concerning the variance, they can be obtained as (and not as $\text{Var} = \mathcal{E}((\bar{u}_i)^2) - (\mathcal{E}(\bar{u}_i))^2$)

$$\text{Var} = \mathcal{E}(\bar{u}_i) - (\mathcal{E}(\bar{u}_i))^2 \quad \forall x_i \in [0,1], \tag{62}$$

because in this specific case ($\bar{u}(x,\xi,t) = 1$)

$$\int_\Xi \bar{u}(x_i,\xi,t)^2 p(\xi)\mathrm{d}\xi = \int_\Xi \bar{u}(x_i,\xi,t) p(\xi)\mathrm{d}\xi = \mathcal{E}(\bar{u}_i). \tag{63}$$

In figure 6, the spatial convergence for the aSI scheme and for the full scheme, employing only the MHM with the superbee limiter (40), are reported for the mean 6(a) and the variance 6(b) (L^2 norms). Similar curves are obtained for L^1 and L^∞ norms but are not reported here for brevity. The computations are performed over equally spaced meshes in the physical space Ω with 51, 101, 201, 401 and 601 points. The aSI scheme is applied with a coarsest level of 16 cells ($m_0 = 4$), a finest level of 256 stochastic cells ($m = 4$) and a threshold equal to $\varepsilon = 10^{-3}$. The polynomial reconstruction is the quadratic polynomial with and without ENO selection of the stencil. The average number of stochastic cells employed is equal to 39 when the ENO selection is employed and to 40 with the centered stencil.

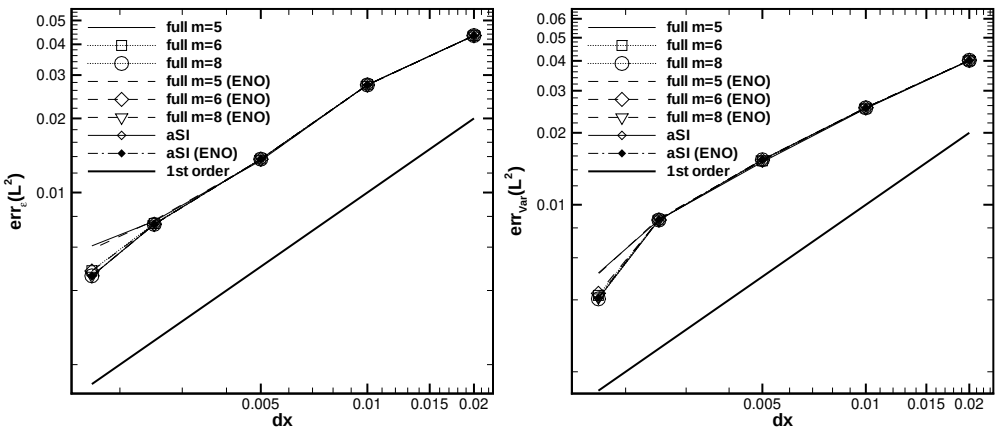

(a) (b)

Figure 6. Spatial convergence for the linear advection problem with discontinuous initial condition (57). The statistics of the solution (mean (a) and variance (b)) obtained with (aSI) and without (full) compression are reported for the MHM method with the superbee limiter (40).

The figure 6 shows that the aSI scheme is able to preserve the accuracy and the order of convergence of the full scheme with a reduction of the computational cost with respect to the

DOI: 10.1002/fld

full solution obtained over a grid of 256 cells ($m = 8$). The aSI scheme requires a computational effort equivalent to a computation carried out on about 40 equally spaced stochastic cells. The full solutions on 32 ($m = 5$) and 64 ($m = 6$) cells are then reported in order to compare the efficiency of the scheme with respect to a solution obtained with a similar computational effort. However, the aSI scheme performs better with respect to both the full solution at 32 and 64 cells. Moreover, the quality with respect to the full solution of 256 cells is only slightly deteriorated. In figures 7 and 8, the statistics of the solution are reported over the entire physical space (the mesh of 601 points) and compared to the exact solution (see (61)) obtained on 2001 equally spaced points in the physical space. The solutions obtained with the full scheme with 32 and 64 stochastic cells exhibit the well-known staircase phenomenon, i.e. in presence of discontinuous solutions the statistics are constituted by a series of *plateau*. The presence of the *plateau* is due to the lower resolution associated to the discretization of the stochastic space with respect to the resolution of the physical space. The staircase phenomenon is more evident for the coarser case (32 cells), reduces slightly with 64 cells, and disappear with 256 cells. The aSI scheme automatically refines the space where a higher resolution is required. The staircase problem disappears by using aSI even if the (average) number of cells employed is lower than 64 (see figure 7(b) and 8(b)).

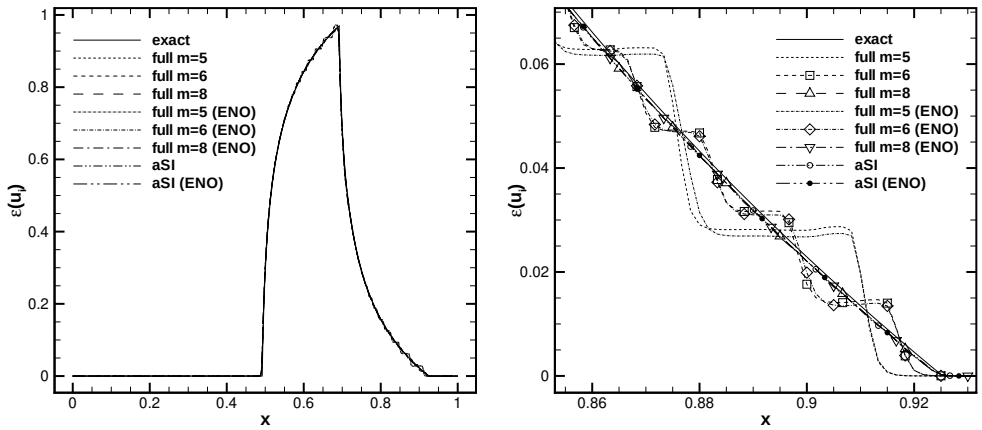

(a) (b)

Figure 7. Expectation for the cell averaged solution of the linear advection equation with discontinuous initial condition (57) at the final time $t = 0.4$. The whole physical domain is represented in (a), while in the figure (b) a zoom in the shock region is reported. The mesh is constituted by 601 equally spaced points.

The ability of aSI scheme to refine only locally the space allows to increase locally the resolution along the stochastic space. In figure 9, the distribution of the stochastic cells over Ω at the final time step $t = 0.4$ is reported. It is evident that the higher computational effort is located in the regions of the strong gradients; comparing the figure 8 and 9, it is evident that the two peaks associated to the local higher computational effort (in terms of stochastic cells) correspond to the two peaks in the variance of the solution. In figure 9, the number of points employed by the aSI scheme with and without the ENO selection of the stencil are also reported. The ENO selection of the stencil reduces the number of cells employed. Moreover, by comparing the average number of stochastic cells employed for each computation, it is evident that the efficiency of the ENO selection increases with the spatial resolution. This is due to the global representation of the solution $u(x, \xi, t)$ over cells $\mathcal{C}_i \times \Xi_j$. Higher is the spatial resolution, sharper are the resulting discontinuities, so the ENO becomes more useful in order to gain in terms of accuracy (with the SI algorithm) and in terms of compression capabilities (with the TE algorithm). Figure 9(b) displays that for too coarse spatial resolution, the ENO selection of the stencil can be negative in terms of both accuracy and

DOI: 10.1002/fld

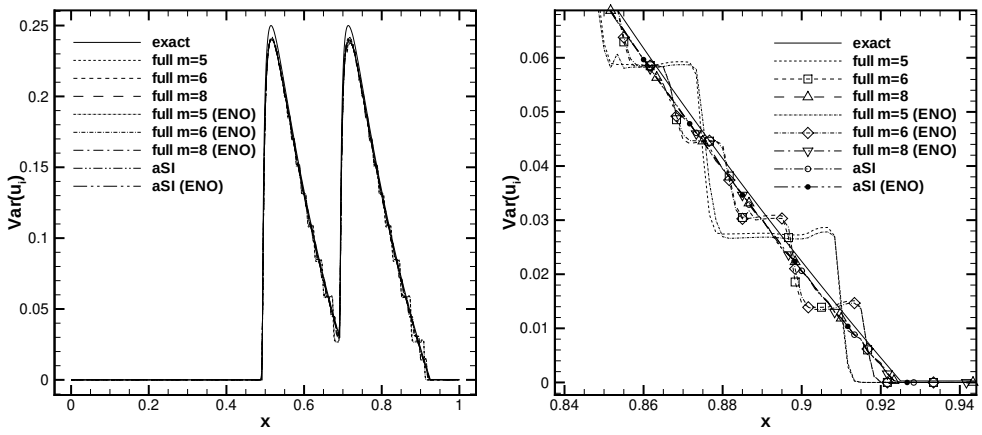

(a) (b)

Figure 8. Variance for the cell averaged solution of the linear advection equation with discontinuous initial condition (57) at the final time $t = 0.4$. The whole physical domain is represented in (a), while in the figure (b) a zoom in the shock region is reported. The physical mesh is constituted by 601 equally spaced points.

compression. The solution becomes smoother and smoother by decreasing the spatial resolution, so a centered stencil becomes the best choice.

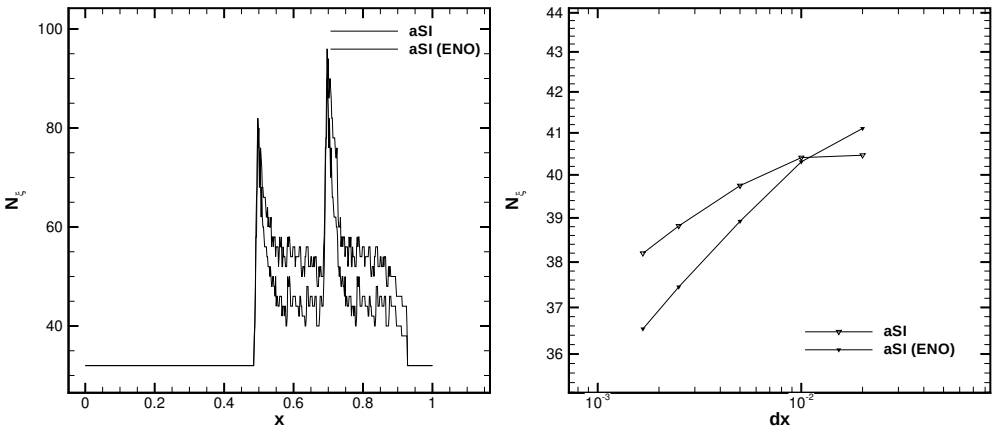

(a) (b)

Figure 9. Evolution of the number of stochastic cells employed in each physical location for the aSI scheme with and without the ENO reconstruction (a) for the linear advection equation with discontinuous initial condition. The average number of stochastic cells, employed by the aSI scheme as a function of the physical space resolution, is reported in (b).

6.2. *Inviscid Burgers equation*

In this section, the aSI algorithm is applied to solve the inviscid Burgers equation

$$\frac{\partial u(x,\xi,t)}{\partial t} + \frac{\partial f(u(x,\xi,t))}{\partial x} = 0 \quad x \in [0,1] \quad \text{and} \quad t \in [0,T], \tag{64}$$

DOI: 10.1002/fld

where the flux function is defined as $f = f(u(x,\xi,t)) = \frac{1}{2}u^2(x,\xi,t)$.

The following uncertain initial condition, with the random parameter uniformly distributed $\xi \sim \mathcal{U}[0,1]$, is prescribed

$$u(x,\xi,0) = \begin{cases} H(\xi) & \text{if} \quad x \in [A_1^x, A_2^x] \\ 0 & \text{if} \quad \text{otherwise.} \end{cases} \tag{65}$$

The initial condition is represented by a hat function with an amplitude dependent (non linearly) on the random parameter, $H(\xi) = \frac{1}{3}\xi^2 + \frac{1}{100}\xi + \frac{9}{10}$. To obtain the exact solution, it is necessary to consider the two elementary solutions of the Riemann problem of the inviscid Burgers equation (see [31] for further details). The first case on the left of the hat function ($x = \frac{1}{10}$) is the Riemann problem with $u_l < u_r$, which admits as solution a rarefaction wave (depending on the uncertainty parameter) as follows

$$u(x,\xi,t) = \begin{cases} 0 & \text{if} \quad x \le A_1^x \\ F(x) & \text{if} \quad x \in [A_1^x, A_1^x + H(\xi)t] \\ H(\xi) & \text{if} \quad x > A_1^x + H(\xi)t, \end{cases} \tag{66}$$

where the solution inside the rarefaction wave is $F(x) = (x + A_1^x)/t$.

By knowing the function $H(\xi)$, the exact solution for the uncertain rarefaction wave can be computed. On the right of the hat ($x = \frac{1}{2}$), the solution of the Riemann problem is a shock wave traveling with an uncertain speed $s = H(\xi)/2$. The complete solution of the Riemann problem is then

$$u(x,\xi,t) = \begin{cases} H(\xi) & \text{if} \quad x < A_2^x + st \\ 0 & \text{if} \quad x > A_2^x + st. \end{cases} \tag{67}$$

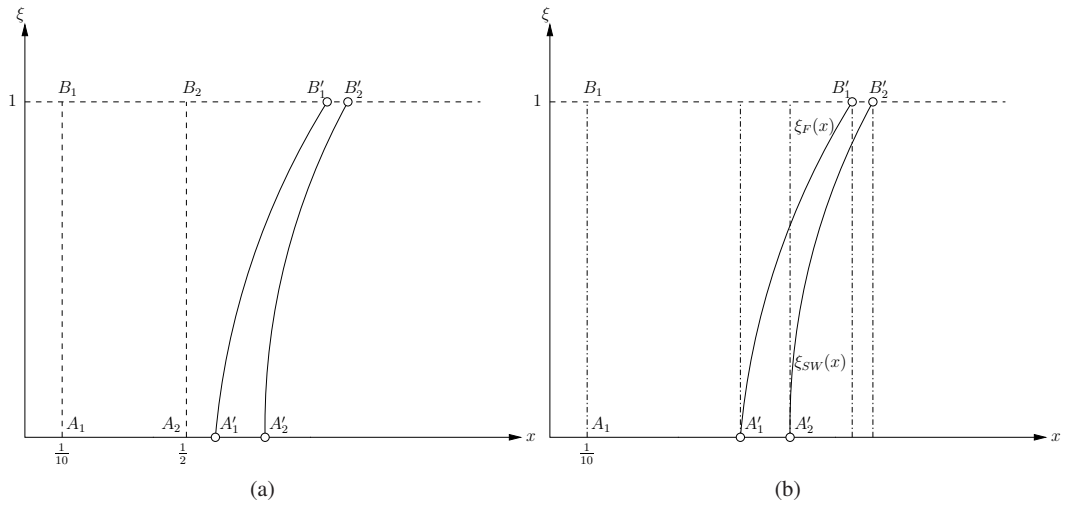

Figure 10. Schematic representation of the evolution between the initial condition (points A_1, A_2, B_1, B_2) and the final condition at time $t = 0.6$ (points A'_1, A'_2, B'_1, B'_2) (a). The regions where the exact solution should be computed, at the final time $t = 0.6$, are reported in (b).

The problem (64) is solved until a time equal to $T = 0.6$, with the initial condition (65) defined by $A_1^x = B_1^x = \frac{1}{10}$ and $A_2^x = B_2^x = \frac{1}{2}$. The solution appears as sketched in figure 10, where the tail of the fan is at rest ($x = \frac{1}{10}$), while the position of the head is a function of the random parameter and its value is bounded between the slower moving fan ($A_1^{\prime,x} = \frac{1}{10} + H(0)t$) and the fast moving one ($B_1^{\prime,x} = \frac{1}{10} + H(1)t$). The random parameter, corresponding to a physical position $x \in [A_1^{\prime,x}, B_1^{\prime,x}]$, can be found after some algebraic manipulations analytically, by solving for ξ the equation $x = A_1^x + H(\xi)t$ for $A_1^{\prime,x} \le x \le B_1^{\prime,x}$, $\xi_F = \xi_F(x)$ (see figure 10 for the locus ξ_F).

DOI: 10.1002/fld

Following a similar procedure, the value of the random parameter corresponding to the shock position $\xi_{SW} = \xi_{SW}(x)$ can be found analytically, by solving for ξ the equation $x = A_2^x + \frac{1}{2}H(\xi)t$ for $A_2^{\prime,x} \leq x \leq B_2^{\prime,x}$.

The statistics of the solution can be computed analytically for each cell $\mathcal{C}_i$ as follows. For the expected value of the physical cell averaged value $\bar{u}_i$

$$\mathcal{E}(\bar{u}_i) = \begin{cases} 0 & \text{if} \quad x_i \leq A_1^x \text{ or } x_i \geq B_2^{\prime,x} \\ F(x_i) & \text{if} \quad x_i \in [A_1, A_1^{\prime,x}] \\ \displaystyle\int_0^{\xi_F(x_i)} H(\xi)\mathrm{d}\xi + F(x_i)(1-\xi_F(x_i)) & \text{if} \quad x_i \in [A_1^{\prime,x}, A_2^{\prime,x}] \\ \displaystyle\int_{\xi_F(x_i)}^{\xi_{SW}(x_i)} H(\xi)\mathrm{d}\xi + F(x_i)(1-\xi_F(x_i)) & \text{if} \quad x_i \in [A_2^{\prime,x}, B_1^{\prime,x}] \\ \displaystyle\int_{\xi_{SW}(x_i)}^{1} H(\xi)\mathrm{d}\xi & \text{if} \quad x_i \in [B_1^{\prime,x}, B_2^{\prime,x}]. \end{cases} \tag{68}$$

All the integrals in the equation (68) can be computed analytically.

Moreover, the variance is easily analytically computed, due to the polynomial behavior of $H(\xi)$, as follows

$$\mathrm{Var}(\bar{u}_i) = \begin{cases} 0 & \text{if} \quad x_i \leq A_1^{\prime,x} \text{ or } x_i \geq B_2^{\prime,x} \\ \displaystyle\int_0^{\xi_F(x_i)} H^2(\xi)\mathrm{d}\xi + F^2(x_i)(1-\xi_F(x_i)) - \mathcal{E}^2(\bar{u}_i) & \text{if} \quad x_i \in [A_1^{\prime,x}, A_2^{\prime,x}] \\ \displaystyle\int_{\xi_F(x_i)}^{\xi_{SW}(x_i)} H^2(\xi)\mathrm{d}\xi + F^2(x_i)(1-\xi_F(x_i)) - \mathcal{E}^2(\bar{u}_i) & \text{if} \quad x_i \in [A_2^{\prime,x}, B_1^{\prime,x}] \\ \displaystyle\int_{\xi_{SW}(x_i)}^{1} H^2(\xi)\mathrm{d}\xi - \mathcal{E}^2(\bar{u}_i) & \text{if} \quad x_i \in [B_1^{\prime,x}, B_2^{\prime,x}]. \end{cases} \tag{69}$$

The (stochastic) inviscid Burgers problem (64) is solved over a set of equally spaced physical meshes with 51, 101, 201, 401 and 601 points. The time space is discretized using 600 time steps of constant length $\Delta t = 1 \times 10^{-3}$. The error norms in L^2, with respect to the exact stochastic solution (see equations (68) and (69)), are reported in figure 11. Similar results are obtained for L^1 and L^∞ norms, but are not reported here for brevity. The reference solution is the full computation performed with the SI scheme and a 256 ($m = 8$) equally spaced stochastic cells. This solution is compressed by means of the aSI scheme with a coarsest level of $m_0 = 4$ and a finest level of $m = 8$ with a threshold equal to $\varepsilon = 10^{-4}$. For both the full SI and the aSI schemes, the computations are performed employing quadratic polynomial reconstruction with and without the ENO selection of the stencil. For each computation, the average number of stochastic cells is evaluated obtaining the equivalent number of equally spaced stochastic cells (with the same computational cost). The evolution of the number of stochastic cells associated to the different (physical) spatial resolutions are reported in figure 14(b) for the aSI scheme with and without the ENO procedure. Moreover, SI scheme is applied over 16 ($m = 4$) and 32 ($m = 5$) equally spaced stochastic cells. These resolutions are chosen because the average number of stochastic cells employed by the aSI scheme varies between these values. The SI scheme (with these spatial resolutions) fails to converge with the expected first order slope both with and without the ENO, because of the appearance of the staircase phenomenon. The stochastic resolution is not high enough with respect to the physical resolution, as evident looking at the three last spatial resolutions in figure 11.

The staircase phenomenon is evident in figures 12 and 13, where the expectation and the variance of the solution are reported over the 601 points physical mesh (the exact solution is evaluated over a mesh of 2001 equally spaced points). In particular, figures 12(b) and 13(b) show a zoom of the curves in the regions where the (uncertain) shock waves propagate (see figure 10). As expected, increasing the number of stochastic cells, even equally spaced, reduces the staircase phenomenon

DOI: 10.1002/fld

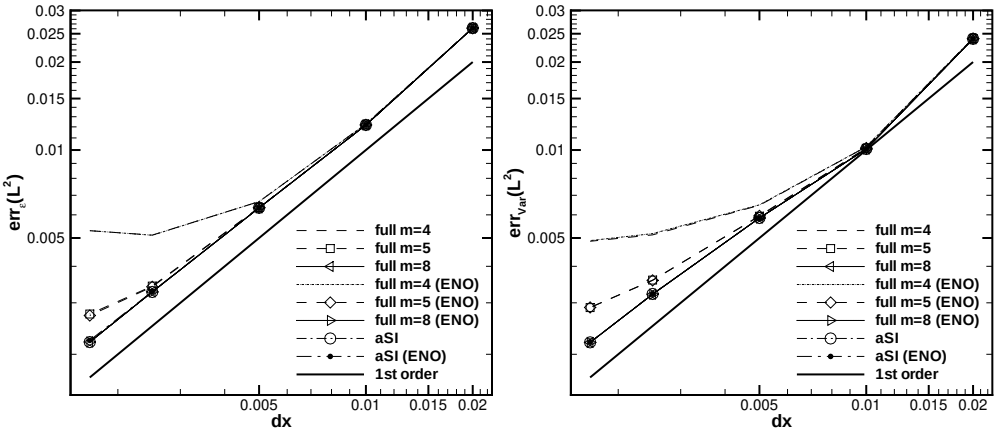

(a) (b)

Figure 11. Spatial convergence for the Burgers equation with an uncertain hat initial condition (65). The statistics of the solution (mean (a) and variance (b)) obtained with (aSI) and without (full) compression are reported for the MHM method with superbee limiter (40).

(from 16 to 32 cells). It disappears with 256 cells. Note that the aSI scheme, with an overall computational cost similar to the two coarse full simulations, yields better results (without the appearance of the staircase phenomenon) concentrating the computational effort, *i.e.* the number of cells, in the regions where the solution is less regular. The capability to refine and coarsen during the simulation following the evolution of the solution in the physical/stochastic space makes the aSI scheme more efficient, yielding results that nearly coincide with the full reference solution.

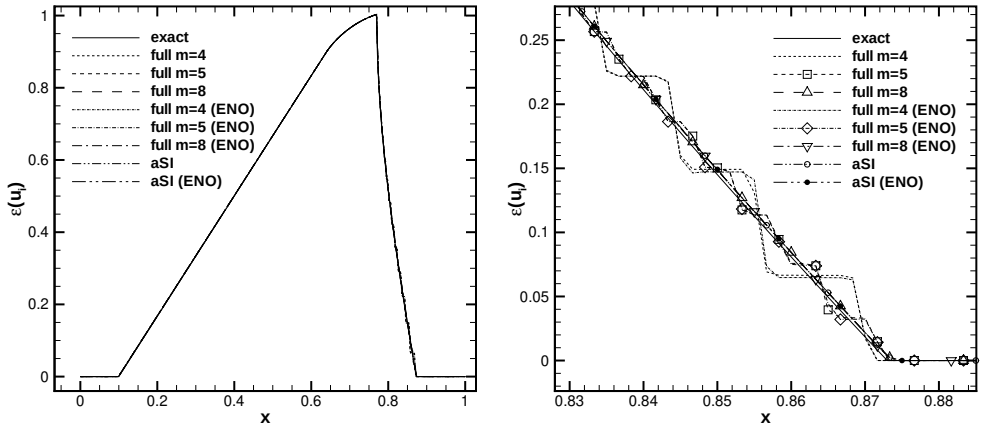

(a) (b)

Figure 12. Expectation for the cell-averaged solution of the inviscid Burgers equation at the final time $t = 0.6$. The whole physical domain is represented in (a), while in figure (b) a zoom in the shock region is reported. The physical mesh is constituted by 601 equally spaced points.

As already discussed for the solution of the linear advection equation with discontinuous initial condition, the presence of the ENO selection of the stencil makes the computations progressively more efficient by increasing the physical resolution. This effect is evident in figure 14(b), where the

DOI: 10.1002/fld

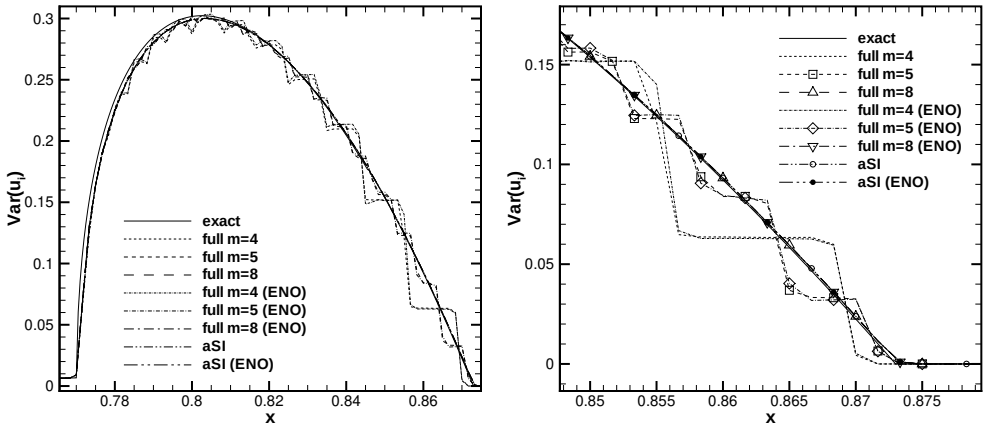

(a) (b)

Figure 13. Variance for the cell-averaged solution of the inviscid Burgers equation at the final time $t = 0.6$. Two different zooms in the shock region are reported. The physical mesh is constituted by 601 equally spaced points.

(average) number of stochastic cells employed is reported as a function of the physical resolution. In figure 14(a), the direct comparison between the aSI scheme with and without the ENO selection of the stencil over the finest 601 points physical mesh is shown. With lower resolution meshes, there is no advantage in using the ENO procedure due to the representation of the solution over cells in the overall physical/stochastic space. However, the slope associated to the average number of stochastic cells shows that the solutions are represented by a narrow discontinuity (due to the increase of the spatial resolution). As a consequence, the non-oscillatory interpolation helps to avoid the so-called *pollution* of the stencil, *i.e.* the propagation of the interpolation error in the neighboring cells of a discontinuity. Again, the combination of the aSI scheme and the use of the ENO procedure for the polynomial interpolation, becomes even more efficient as the spatial resolution is increased. This is a desired property for any intrusive UQ scheme.

In the following section, the aSI scheme is applied to non linear system of stochastic partial differential equations.

6.3. Uncertain shock tube

In this section, the solution of the uncertain shock tube problem is considered. The problem can be modeled by the well-known 1D Euler equations

$$\frac{\partial \mathbf{u}}{\partial t} + \nabla \cdot \mathbf{f}(\mathbf{u}) = \mathbf{0}, \tag{70}$$

where the vector of conservative variables, the density ρ, the momentum $m = \rho u$ and the total Energy E^t, $\mathbf{u} \in \mathbb{R}^3$ and the flux vector $\mathbf{f}(\mathbf{u}) \in \mathbb{R}^3$ are

$$\mathbf{u} = \begin{pmatrix} \rho \\ m \\ E^t \end{pmatrix} \quad \mathbf{f}(\mathbf{u}) = \begin{pmatrix} m \\ \dfrac{m^2}{\rho} + \Pi(\mathbf{u}) \\ \dfrac{m}{\rho}\left(E^t + \Pi(\mathbf{u})\right). \end{pmatrix} \tag{71}$$

DOI: 10.1002/fld

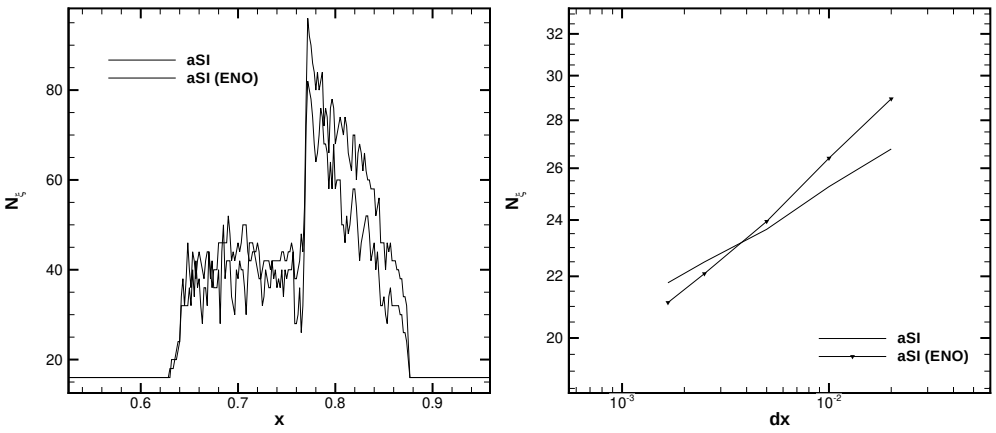

(a) (b)

Figure 14. Evolution of the number of stochastic cells employed for each physical location for the aSI scheme with and without the ENO reconstruction (a) (Inviscid Burgers equation). The average number of stochastic cells employed by the aSI scheme as a function of the physical space resolution is reported in (b).

The pressure $\Pi(\mathbf{u})$ (as function of the conservative variables) can be derived for a polytropic ideal gas as follows

$$\Pi(\mathbf{u}) = (\gamma - 1)\left(E^t - \frac{1}{2}\frac{|m^2|}{\rho}\right). \tag{72}$$

The initial condition for the uncertain shock tube problem is derived from the classical Sod test case [34], where an uncertainty of the density at the left state ($x < x_d$ for $t = 0$) is introduced:

$$\mathbf{u}_L(x,\xi,t) = \begin{pmatrix} \rho_L(\xi) \\ 0 \\ \dfrac{p_L}{\gamma - 1} \end{pmatrix} \quad \mathbf{u}_R(x,\xi,t) = \begin{pmatrix} \rho_R \\ 0 \\ \dfrac{p_R}{\gamma - 1}. \end{pmatrix}, \tag{73}$$

In particular, the density on the left state is dependent on an uniformly distributed random parameter $\xi \sim \mathcal{U}[0,1]$: $\rho_L(\xi) = 0.3 + 1.6\xi$. The values of the pressures are $p_L = 1$ and $p_R = 0.1$, while the right value of the density is $\rho_R = 0.125$. The total energy E^t is obtained (considering the gas at the rest in the whole domain) as a function of the local pressure and the ratio between specific heats, that for a diatomic gas can be assumed equal to $\gamma = 1.4$.

As pointed out by Toro [32], analyzing the eigenvalue structure of the Euler equations, the Riemann problem for the 1D Euler equations (see figure 15) generates (for $t > 0$) four states, where two are not known (variables are indicated with a star in the following). The Riemann problem for the solution of the 1D Euler equation can be reduced to the solution of a single non-linear algebraic equation for the pressure in the star region $p^\star$ from which the other quantities can be computed. With an uncertain shock tube problem, the dependence of $p^\star$ on the random parameter $p^\star = p^\star(\xi)$ should be considered. Unfortunately, this dependence cannot be computed explicitly. In this paper, only the case involving a left moving rerefaction fan and a right moving shock wave are considered. Moreover, initial conditions (73) produce this wave structure for all the random parameter taken into account. The problem is further complicated by the presence of complex functions that should be integrated to compute the exact statistics required. The solution strategy employed is the following. For each physical location, where the exact statistics should be computed, the solution along the stochastic space is divided into smooth regions (where the numerical quadrature with a large number of points produces fair well-converged results even for non-polynomial functions). The main issue

DOI: 10.1002/fld

is to determine the location of a discontinuity. This task can be accomplished solving an algebraic non-linear equation for the random parameter that can be formulated to involve all (but not only) the derivative available for the solution of the deterministic Riemann problem. After the subdivision of the random space in more regions, where the quadrature can be done numerically without accuracy loss (to the desired global accuracy), the statistics are computed in order to obtain the desired reference solutions.

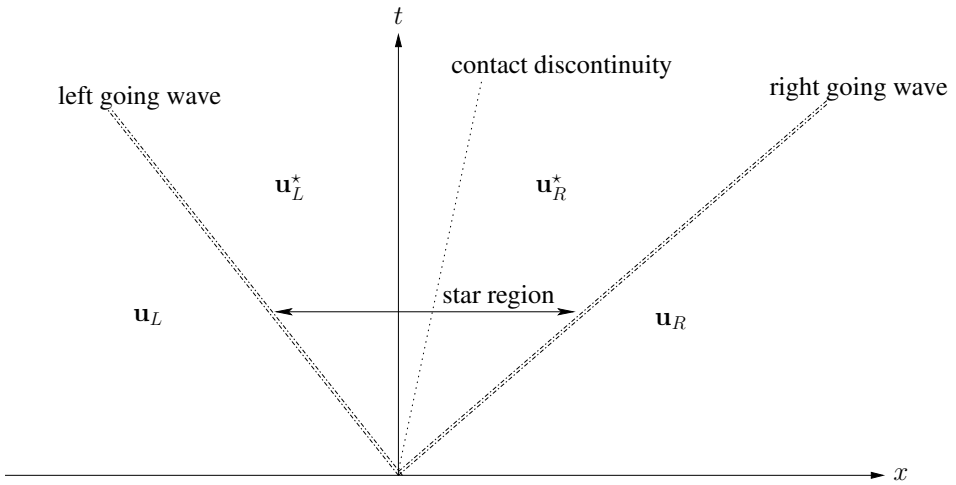

Figure 15. Riemann wave structure for the 1D Euler equation.

Details of the numerical procedure to obtain the reference solution of the stochastic Riemann problem are reported in the Appendix .1.

Simulations are performed over a physical domain $\Omega = [-\frac{1}{5}, \frac{6}{5}]$ until a final time $t = 0.31$ with the position of the diaphragm equal to $x_d = 0.42$. The time space is divided in 6200 equal time steps of length $\Delta t = 5 \times 10^{-5}$. The simulations are carried out over equally spaced meshes of 201, 401, 801 and 1001 points employing the aSI scheme based on the MHM with a van Leer limiter (see equation (41)).

In figure 16, the spatial convergence is reported for both the mean (16(a)) and the variance (16(b)) in L^2 for the density ρ. The aSI method is applied with a coarsest level of 4 ($m_0 = 2$) cells and a finest level of 256 ($m = 8$) stochastic cells with $\varepsilon = 10^{-4}$, while the reference solution is the full SI scheme with 256 cells. The aSI scheme has used an average number of stochastic cells between the two levels $m = 5$ and $m = 6$ (see figure 19(b)), so the other solutions are computed by means of the SI scheme for comparison. For all the schemes, both the centered second order polynomial reconstruction and the non-linear ENO one are used. The difference between the two polynomial reconstructions is difficult to appreciate because the spatial resolution is too poor for a sharp representation of the discontinuities. In this sense, there is no advantage in using the ENO reconstruction (for the aSI scheme and the SI scheme). The first order of convergence is attained for the expectation of the density ρ, while, even with the SI scheme, the variance exhibits a lower rate of convergence 16(b). This behavior clearly indicates that even the solution employing 256 stochastic cells is not fully converged for moments higher than the expectation.

However, the aSI scheme displays the required properties: it saves the order of accuracy of the full SI scheme, both for mean and variance (see figure 16), and the degradation of the accuracy (with respect to the full scheme) is strongly limited. Moreover, as already shown in the previous numerical results, the phenomenon of the staircase approximation of the statistics is prevented by the adaptation in the stochastic space. As shown in figure 17, note that all the numerical solutions are very similar to the exact solution 17(a) obtained over a mesh of 2001 equally spaced points in the physical space. By zooming (17(b)), the presence of the typical staircase phenomenon for both the SI scheme with 32 and 64 stochastic cells appears. The solution obtained with the aSI scheme agrees very well with its full counterparts.

DOI: 10.1002/fld

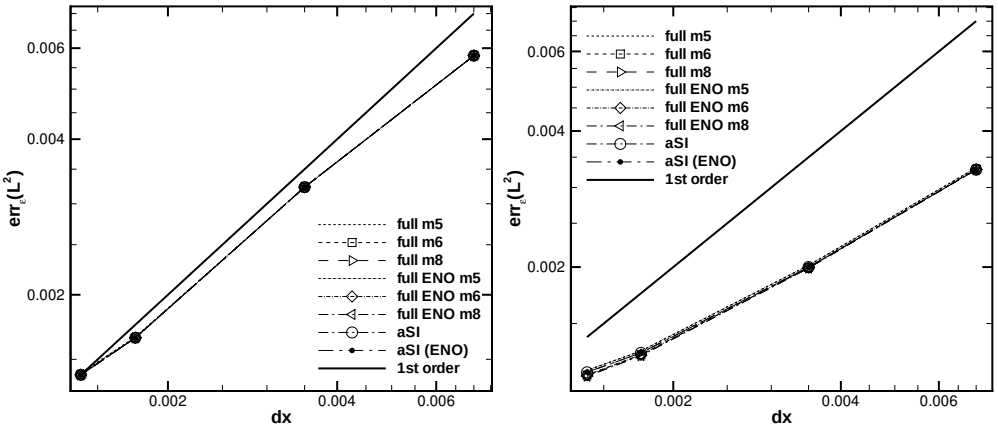

(a) (b)

Figure 16. Spatial convergence for the stochastic shock tube problem equation with uncertain initial condition (73). The statistics of the solution (mean (a) and variance (b)) obtained with (aSI) and without (full) compression are reported for the MHM method with van Leer limiter (41).

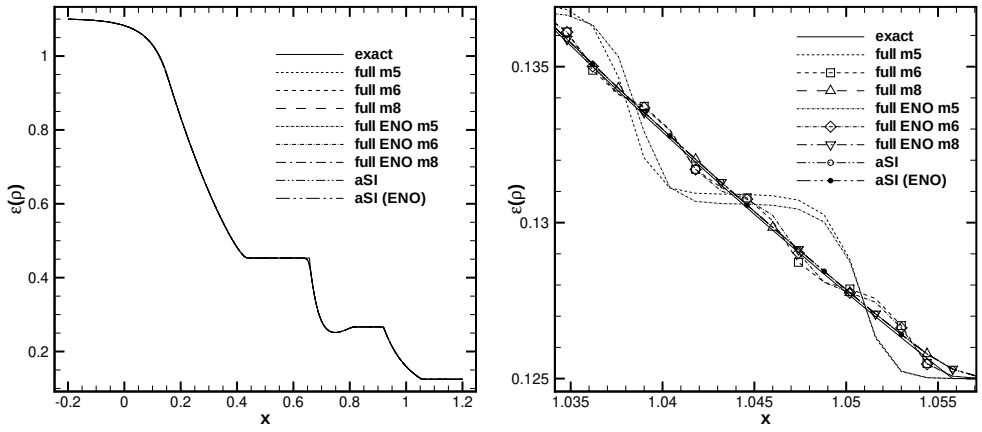

(a) (b)

Figure 17. Density Expectation for the cell averaged solution of the uncertain shock tube problem at the final time $t = 0.31$. The whole physical domain is represented in (a), while in the figure (b) a zoom in the shock region is reported. The physical mesh is constituted by 1001 equally spaced points.

As already demonstrated for the mean, even for the variance, the presence of the staircase approximation is prevented by the refinement of the stochastic space (see figure 18). Even if curves nearly coincide in figure 18(a), in the shock region the presence of the typical step pattern is evident for the full SI solution with 32 and 64 equally spaced stochastic cells (see 18(b)).

The lower order of convergence attained for the variance, even for the non compressed solution, highlights that the error in the stochastic space influences the global error. As already demonstrated, the efficiency of the ENO selection of the stencil is related to the sharp representation of the discontinuities. In this case, the results with and without the ENO selection of the stencil are very similar. No advantages, even in terms of compression, are observed. This issue is evident in figure 19(a), where the number of stochastic cells, along the physical domain, are reported. The region

DOI: 10.1002/fld

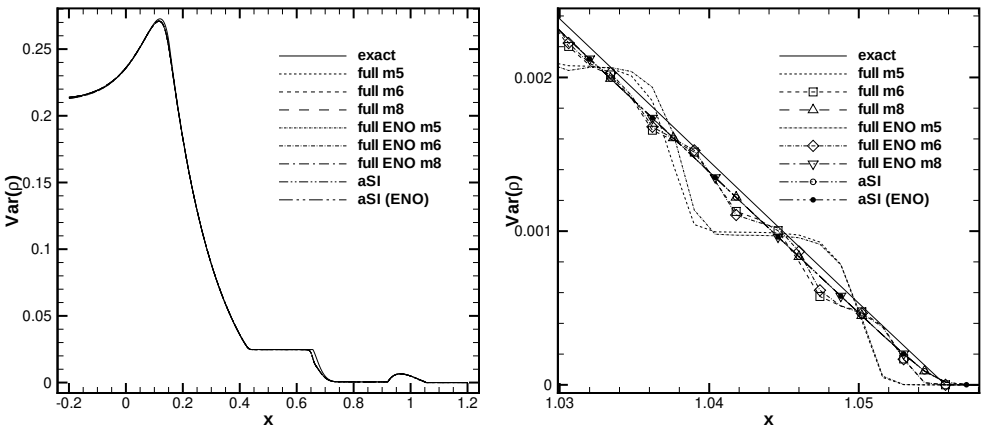

(a) (b)

Figure 18. Density Variance for the cell averaged solution of the uncertain shock tube problem at the final time $t = 0.31$. The whole physical domain is represented in (a), while in the figure (b) a zoom in the shock region is reported. The physical mesh is constituted by 1001 equally spaced points.

associated to the discontinuity spreads over a larger domain and, globally, the presence of non-centered stencils deteriorates the quality of prediction. This issue is well known in the ENO literature [21]. A possible cure, outside the scope of the present paper, would be the introduction of WENO type of interpolation. Employing a WENO type of interpolation, the correct centered stencil could be recovered without strong degradation of the prediction (the authors already introduced a WENO interpolation in [11] in the context of the TE point-value setting).

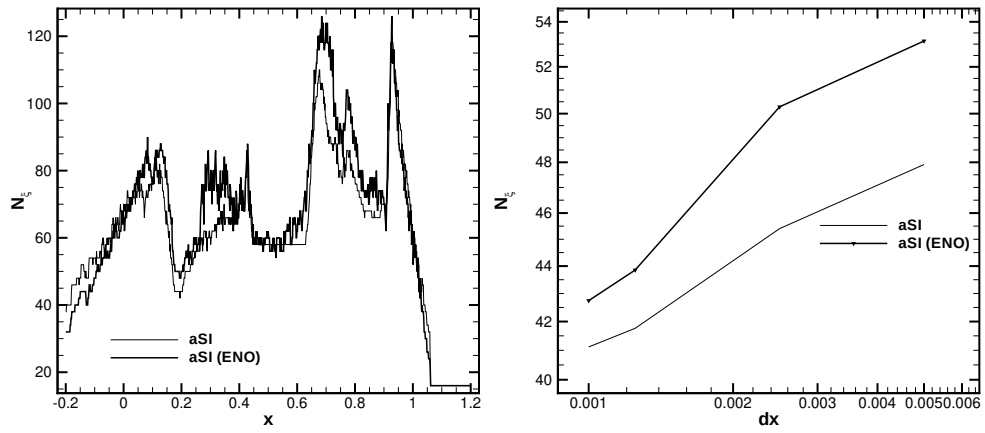

(a) (b)

Figure 19. Evolution of the number of stochastic cells employed for each physical location for the aSI scheme with and without the ENO reconstruction (Shock tube problem). The average number of stochastic cells employed by the aSI scheme as function of the physical space resolution has been reported in (b).

The evolution of the average number of stochastic cells employed by the aSI scheme with and without the ENO interpolation is reported in 19(b). In this case, there is no intersection between

DOI: 10.1002/fld

the two curves, revealing that in this case the ENO interpolation gives no advantage, even for high physical space resolutions.

7. CONCLUDING REMARKS

In this paper, a novel adaptive intrusive numerical scheme for Uncertainty Quantification has been presented. In particular, the TE framework [15, 10, 11] has been extended to include the dependence on a generic probability density function, in a cell-average setting and employing non-linear high-order reconstructions, . The aim is to obtain, at the same time, a saving in memory requirements and in the computational cost associated to the evaluations of the system. This general algorithm has been coupled with the Semi-Intrusive (SI) scheme for UQ proposed by Abgrall and co-workers [7, 8]. The overall numerical scheme is the so-called adaptive-SI scheme. It has been demonstrated that it preserves the convergence properties of the original SI scheme with strong savings in terms of computational cost. Different test-cases have been presented to demonstrate the efficiency and the accuracy properties of the aSI scheme. The linear advection equation has been solved for initial smooth and discontinuous solution to demonstrate the capability of the stochastic scheme to preserve the accuracy related to the deterministic scheme. A second test-case has been focused on the inviscid Burgers equation. The method permits to automatically refining/coarsening the tessellation following the evolution in time of the regularity of the solution in the coupled stochastic/physical space. In particular, a smooth solution has been considered, in the stochastic space, as initial condition, where shock waves velocities are directly related to the parameter in the stochastic space. The final test case proposed has been the uncertain shock tube problem. The aSI scheme has been demonstrated to be efficient also in the case of vectorial problems. For the computation of the convergence curves, an original strategy for the semi-analytical solution of the stochastic shock tube problem has been also developed following and extending the classical numerical procedure for the solution of the Riemann problem for the Euler equations. This paper constitutes the first effort to introduce a MR framework into the SI method. The generality of the approach is not limited to second order scheme, but can be easily extended to higher order numerical formulation for the physical space and time discretizations. In the present work, both the linear and non-linear MR framework have been presented, in which the selection of the stencil for the reconstruction operators can be obtained by a data-dependent procedure: the ENO selection of the stencil has been introduced. Considering the numerical results presented, note that the advantages related to the non-linear schemes are very limited. This issue is related not to the non-linear procedure itself but to the peculiarity of the SI scheme that produces representations of the solution in a combined physical stochastic space. The representation of discontinuous solution along the stochastic space can recover a smoother behavior, when the physical spatial resolution is not high enough. This has been demonstrated by showing that the importance of the ENO scheme increases with the physical space resolution. To improve the global properties of the scheme, two further steps seem useful. The first is the introduction of the WENO reconstruction instead of the ENO interpolation recovering the correct stencil in all the regions where the solution is smooth, as it has been already presented for the point-value setting [11]. The other step could be to increase the polynomial order for the reconstruction. This should improve both accuracy and compression capabilities. The extension and the analysis of the aSI scheme for a higher number of dimension is actually underway.

ACKNOWLEDGEMENT

The authors acknowledge the two anonymous referees for their invaluable comments. Rémi Abgrall and Gianluca Geraci have been supported by the ERC Advanced Grant ADDECCO N°226316. The authors greatly acknowledge also the Associated Team AQUARIUS (Joint team from INRIA and Stanford University).

.1. *Accurate numerical solution for the 1D stochastic Riemann problem for the Euler equations*

In this section, the numerical procedure to obtain the reference solution for the stochastic shock tube problem is illustrated (the interesting reader may refer to [32] for a complete description of the deterministic problem). Let us consider a deterministic Riemann problem for the 1D Euler equations, in particular the case of a left going rarefaction wave and a right moving shock wave. This assumption do not pose any limitation on the general procedure for the solution of the stochastic problem presented here.

The solution of the deterministic Riemann problem (for gas initially at the rest) consists in solving a non-linear equation for the pressure in the region between the shock and the contact discontinuity. Remark that each quantity is here dependent on the random parameter. In the deterministic case, the random parameter is obviously assumed as a constant. In the following, the explicit dependence of each quantity with respect the random parameter ξ is explicitly reported for the uncertain initial left state (see equation (73)). However, the dependence of all the quantities from the random parameter must be considered redundant if the deterministic case is of interest because in that case all the uncertain parameters assume a fixed value. The non-linear equation to solve for the pressure in the star region $p^\star$ is the following

$$\begin{aligned} f(p^\star(\xi),\mathbf{u}_L(\xi),\mathbf{u}_R) &= f_L(p^\star(\xi),\mathbf{u}_L(\xi)) + f_R(p^\star(\xi),\mathbf{u}_R) \\ &= \frac{2a_L(\xi)}{\gamma-1}\left[\left(\frac{p^\star(\xi)}{p_L}\right)^{\frac{\gamma-1}{2\gamma}} - 1\right] + \left(p^\star(\xi)-p_R\right)\left[\frac{\frac{2}{(\gamma+1)\rho_R}}{p^\star(\xi)+\frac{\gamma-1}{\gamma+1}p_R}\right]^{\frac{1}{2}} = 0, \end{aligned} \tag{74}$$

with the speed of sound $a_L(\xi) = \sqrt{\gamma\frac{p_L}{\rho_L(\xi)}}$.

The equation (74) is solved by means of an iterative Newton-Raphson scheme following [32]

$$\begin{cases} \Delta p^\star = -\left(\dfrac{\mathrm{d}f(p^\star(\xi),\mathbf{u}_L(\xi),\mathbf{u}_R)}{\mathrm{d}p^\star}\Big|_{p^\star(\xi)=p_k^\star(\xi)}\right)^{-1} f(p_k^\star(\xi),\mathbf{u}_L(\xi),\mathbf{u}_R) \\ p_{k+1}^\star(\xi) = p_k^\star(\xi) + \Delta p^\star. \end{cases} \tag{75}$$

The initial condition is systematically $p_0^\star = \frac{p_L+p_R}{2}$) and $\Delta p^\star \leq 10^{-14}$ is chosen as convergence criterion. Derivative of the function $f(p^\star(\xi),\mathbf{u}_L(\xi),\mathbf{u}_R)$ with respect to $p^\star$ can be computed as follows

$$\begin{cases} \dfrac{\mathrm{d}f(p^\star(\xi),\mathbf{u}_L(\xi),\mathbf{u}_R)}{\mathrm{d}p^\star(\xi)} = \dfrac{\mathrm{d}f_L(p^\star(\xi),\mathbf{u}_L(\xi))}{\mathrm{d}p^\star} + \dfrac{\mathrm{d}f_R(p^\star(\xi),\mathbf{u}_R)}{\mathrm{d}p^\star} \\ \dfrac{\mathrm{d}f_L(p^\star(\xi),\mathbf{u}_L(\xi))}{\mathrm{d}p^\star} = \dfrac{1}{\gamma p^\star(\xi)}\sqrt{\gamma\dfrac{p_L}{\rho_L}}\left(\dfrac{p^\star(\xi)}{p_L}\right)^{\frac{\gamma-1}{2\gamma}} \\ \dfrac{\mathrm{d}f_R(p^\star(\xi),\mathbf{u}_R)}{\mathrm{d}p^\star} = \dfrac{2}{(\gamma+1)\rho_R\left(p^\star(\xi)+\frac{\gamma-1}{\gamma+1}p_R\right)}\left[1-\dfrac{(p^\star(\xi)-p_R)}{\left(p^\star(\xi)+\frac{\gamma-1}{\gamma+1}p_R\right)}\right]. \end{cases} \tag{76}$$

Once computed the pressure $p^\star$, the particle velocity $u^\star$ can be computed according to

$$u^\star(\xi) = \frac{1}{2}\left(f_R(p^\star(\xi),\mathbf{u}_R) - f_L(p^\star(\xi),\mathbf{u}_L(\xi))\right), \tag{77}$$

while the density in the star region is defined as

$$\begin{aligned} \rho_L^\star(\xi) &= \rho_L(\xi)\left(\frac{p^\star(\xi)}{p_L}\right)^{\frac{1}{\gamma}} \\ \rho_R^\star(\xi) &= \rho_R\left[\frac{\frac{p^\star(\xi)}{p_R}+\frac{\gamma-1}{\gamma+1}}{\frac{\gamma-1}{\gamma+1}\frac{p^\star(\xi)}{p_R}+1}\right]. \end{aligned} \tag{78}$$

Now, let us determine the positions of the rarefaction wave, of the contact discontinuity and of the shock wave. In the following, HF, TF, CD and SW are used to name the head and tail of the rarefaction fan, the contact discontinuity and the shock waves respectively. These coordinates can be computed only as a function of the variable in the star region, $p^\star$ and $u^\star$, and of the left and right states $\mathbf{u}_L$ and $\mathbf{u}_R$ at a certain

DOI: 10.1002/fld

time t:

$$\begin{cases} \mathrm{HF}(\xi,t) = x_d - a_L(\xi)t \\ \mathrm{TF}(\xi,t) = x_d - (u^\star(\xi) - a_L^\star(\xi))t \\ \mathrm{CD}(\xi,t) = x_d + u^\star(\xi)t \\ \mathrm{SW}(\xi,t) = x_d + a_R\left[\dfrac{\gamma+1}{2\gamma}\dfrac{p^\star(\xi)}{p_R} + \dfrac{\gamma-1}{2\gamma}\right] \end{cases} \quad \text{where} \quad \begin{cases} a_L(\xi)^\star = a_L(\xi)\left(\dfrac{p^\star(\xi)}{p_L}\right)^{\frac{\gamma-1}{2\gamma}} \\ a_R = \sqrt{\gamma\dfrac{p_R}{\rho_R}}. \end{cases} \tag{79}$$

The complete solution of the Riemann problem is then (see also figure 20)

$$\mathbf{u}(x,\xi,t) = \begin{cases} \mathbf{u}_L(x,\xi,t) & \text{if} \quad x < \mathrm{HF}(\xi,t) \\ \mathbf{u}_F(x,\xi,t) & \text{if} \quad \mathrm{HF}(\xi,t) < x < \mathrm{TF}(\xi,t) \\ \mathbf{u}_L^\star(x,\xi,t) & \text{if} \quad \mathrm{TF}(\xi,t) < x < \mathrm{CD}(\xi,t) \\ \mathbf{u}_R^\star(x,\xi,t) & \text{if} \quad \mathrm{CD}(\xi,t) < x < sw(\xi,t) \\ \mathbf{u}_R(x,\xi,t) & \text{if} \quad x > \mathrm{SW}(\xi,t), \end{cases} \tag{80}$$

where the solution inside the rarefaction fan is as follows

$$\mathbf{u}_F(x,\xi,t) = \begin{bmatrix} \rho_L(\xi)\left[\dfrac{2}{\gamma+1} - \dfrac{\gamma-1}{a_L(\xi)(\gamma+1)}r(x,t)\right]^{\frac{2}{\gamma-1}} \\ \dfrac{2\rho_L(\xi)}{\gamma+1}\left[a_L(\xi) + r(x,t)\right] \\ \dfrac{p_L}{\gamma-1}\left[\dfrac{2}{\gamma+1} - \dfrac{\gamma-1}{a_L(\xi)(\gamma+1)}r(x,t)\right]^{\frac{2\gamma}{\gamma-1}} \end{bmatrix} = \begin{bmatrix} \rho_F(\xi) \\ m_F(\xi) \\ E^t(\xi) \end{bmatrix}, \tag{81}$$

while in the star region

$$\mathbf{u}_L^\star(x,\xi,t) = \begin{bmatrix} \rho_L^\star(\xi) \\ \rho_L^\star(\xi)u^\star(\xi) \\ \dfrac{p^\star(\xi)}{\gamma-1} \end{bmatrix} \quad \text{and} \quad \mathbf{u}_R^\star(x,\xi,t) = \begin{bmatrix} \rho_R^\star(\xi) \\ \rho_R^\star(\xi)u^\star(\xi) \\ \dfrac{p^\star(\xi)}{\gamma-1} \end{bmatrix}. \tag{82}$$

A similarity variable $r(x,t)$, defined as $r(x,t) = \frac{x-x_d}{t}$, is introduced.

Note that if a value for the random parameter is fixed, the previous procedure coincide with the classical solution of the Riemann problem as reported in [32]. However, here the interest is the computations of the statistics, the expectation and the variance, of the solution $u(x,\xi,t)$. To obtain the statistics, the solution $u(x,\xi,t)$ has to be integrated numerically splitting the random space. In particular, the integration is carried out by dividing the computational domain of the stochastic space according to (80). The complete solution of the stochastic Riemann problem for the Euler equation using the initial conditions (73), consists in capturing four structures: the region of points describing the position of the head and tail of the rarefaction wave, the contact discontinuity and the shock wave. For each zone, it is necessary to find the random parameter

$$\xi_d : x = g(\xi_d, t) \quad \forall (x,t) \in \Omega \supseteq D(t) \times T, \tag{83}$$

where the function $g(\xi,t)$ can be one of the region reported in (79). It is assumed here that functions g are monotone functions with respect to the random parameter. The subset of the physical space $D(t)$ can be defined considering the union of all the images of the functions describing the physical position of the discontinuities

$$D(t) = [\mathrm{HF}_{\min}(t), \mathrm{HF}_{\max}(t)] \cup [\mathrm{TF}_{\min}(t), \mathrm{TF}_{\max}(t)] \cup [\mathrm{CD}_{\min}(t), \mathrm{CD}_{\max}(t)] \cup [\mathrm{SW}_{\min}(t), \mathrm{SW}_{\max}(t)]. \tag{84}$$

Note that for each (x,t), more than one ξ_d corresponding to the intersections with different regions could exist, but not multiple intersections with the same region. The case of multiple intersections is determined by a non-null intersection between two or more images of the g functions. The monotonicity of the g function implies that the extrema of g correspond to the bounds of the stochastic space. This property is useful from a practical point of view because for each time step the domain $D(t)$ can be easily determined by (84).

Intersections should be computed solving the non-linear algebraic equations (83) by using Newton-Raphson techniques. Let us focus now on the four regions.

DOI: 10.1002/fld

The intersection between the line x and the head fan $\mathrm{HF}(\xi,t)$ can be obtained as follows

$$x = \mathrm{HF}(\xi,t) = x_d - a_L t = x_d - \sqrt{\gamma \frac{p_L}{\rho_L(\xi)}} \quad \rightarrow \quad \rho_L(\xi) = \frac{\gamma p_L}{r^2(x,t)}. \tag{85}$$

If density ρ_L is linearly dependent on the random parameter $\xi \sim \mathcal{U}[0,1]$ (as presented in section 6.3) the value of the intersection is equal to

$$\xi_d = \frac{1}{\rho_L(1) - \rho_L(0)} \left(\frac{\gamma p_L}{r^2(x,t)} - \rho_L(0) \right). \tag{86}$$

Concerning the tail of the rarefaction wave, it follows that

$$x = x_d + \left(\frac{1}{2} \left[f_r(p^\star(\xi),\xi) - f_L(p^\star(\xi),\xi) \right] - a_L(\xi) \left(\frac{p^\star(\xi)}{p_L} \right)^{\frac{\gamma-1}{2\gamma}} \right) t \tag{87}$$

where both functions f_L and f_R are dependent on the random parameter (omitting the dependence from the left $\mathbf{u}_L(\xi)$ and right states $\mathbf{u}_R$).

The problem is to find the root of the function $F(p^\star(\xi),\xi)$

$$\begin{aligned} F(p^\star(\xi),\xi) &= r(x,t) - f_R(p^\star(\xi)) + \sqrt{\gamma \frac{p_L}{\rho_L(\xi)}} \left(\frac{p^\star(\xi)}{p_L} \right)^{\frac{\gamma-1}{2\gamma}} \\ &= r(x,t) - f_R(p^\star(\xi)) + C(p^\star(\xi),\xi) = 0, \end{aligned} \tag{88}$$

where the relation (77) is injected in the previous equation.

The iterative procedure for the solution of (88) is the following

$$\begin{cases} \Delta\xi = -\left(\dfrac{\mathrm{d}F(p^\star(\xi),\xi)}{\mathrm{d}\xi}\Big|_{\xi=\xi_k} \right)^{-1} F(p^\star(\xi_k),\xi_k)) \\ \xi_{k+1} = \xi_k + \Delta\xi, \end{cases} \tag{89}$$

where the differential is equal to

$$\begin{aligned} \frac{\mathrm{d}F(p^\star(\xi),\xi)}{\mathrm{d}\xi} &= \frac{\partial F(p^\star(\xi),\xi)}{\partial \xi} + \frac{\partial F(p^\star(\xi),\xi)}{\partial p^\star} \frac{\mathrm{d}p^\star(\xi)}{\mathrm{d}\xi} \\ &= \frac{\partial C(p^\star(\xi),\xi)}{\partial \xi} + \left(-\frac{\mathrm{d}f_R(p^\star(\xi))}{\mathrm{d}p^\star} + \frac{\partial C(p^\star(\xi),\xi)}{\partial p^\star} \right) \frac{\mathrm{d}p^\star(\xi)}{\mathrm{d}\xi}. \end{aligned} \tag{90}$$

The derivative of the function $C(p^\star(\xi),\xi)$ has to be computed as well as the derivative $\dfrac{\mathrm{d}p^\star(\xi)}{\mathrm{d}\xi}$, while $\dfrac{\mathrm{d}f_R(p^\star(\xi))}{\mathrm{d}p^\star}$ is already available (see equation (76)).

The derivatives of $C(p^\star(\xi),\xi)$ are

$$\begin{aligned} \frac{\partial C(p^\star(\xi),\xi)}{\partial \xi} &= -\frac{1}{2} \frac{\left(\frac{p^\star(\xi)}{p_L} \right)^{\frac{\gamma-1}{2\gamma}} \gamma p_L \left(\rho_L(1) - \rho_L(0) \right)}{\rho_L^2(\xi) \sqrt{\gamma \frac{p_L}{\rho_L(\xi)}}} \\ \frac{\partial C(p^\star(\xi),\xi)}{\partial p^\star} &= \frac{1}{2} \frac{\sqrt{\gamma \frac{p_L}{\rho_L(\xi)}} \left(\frac{p^\star(\xi)}{p_L} \right)^{\frac{\gamma-1}{2\gamma}} (\gamma - 1)}{\gamma p^\star(\xi)}, \end{aligned} \tag{91}$$

while, at each time step, the derivative $\dfrac{\mathrm{d}p^\star(\xi)}{\mathrm{d}\xi}$ can be approximated by means of a backward difference

$$\frac{\mathrm{d}p^\star(\xi)}{\mathrm{d}\xi} \simeq \frac{p^\star(\xi_{k+1}) - p^\star(\xi_k)}{\xi_{k+1} - \xi_k}, \tag{92}$$

since $p^\star$ is not known explicitly.

DOI: 10.1002/fld

From a practical point of view, the initial guess ξ_0 is chosen as the solution of the linear approximation for $\mathrm{TF}(\xi,t)$ between the extrema of the stochastic domain, with $\dfrac{\mathrm{d}p^\star(\xi_0)}{\mathrm{d}\xi} = 0.1$.

Considering the intersection with the contact discontinuity, it follows that

$$\begin{aligned} F(p^\star(\xi),\xi) &= r(x,t) - u^\star(\xi) \\ &= r(x,t) - \frac{1}{2}\left(f_R(p^\star(\xi)) - f_L(p^\star(\xi),\xi)\right) = r(x,t) - f_R(p^\star(\xi)) = F(p^\star). \end{aligned} \tag{93}$$

The iterative procedure is formally equal to (89) (even if here the dependence is not explicit with respect to ξ), with a different differential term

$$\begin{aligned} \frac{\mathrm{d}F(p^\star(\xi))}{\mathrm{d}\xi} &= \frac{\mathrm{d}F(p^\star(\xi))}{\mathrm{d}p^\star}\frac{\mathrm{d}p^\star(\xi)}{\mathrm{d}\xi} \\ &= -\frac{\mathrm{d}f_R(p^\star(\xi))}{\mathrm{d}p^\star}\frac{\mathrm{d}p^\star(\xi)}{\mathrm{d}\xi}. \end{aligned} \tag{94}$$

This differential can be computed according to (76) and (92).

Finally, the intersection with the shock waves is demanded. The non linear algebraic equation results

$$\begin{aligned} F(p^\star(\xi),\xi) &= r(x,t) - a_R\left[\frac{\gamma+1}{2\gamma}\frac{p^\star}{p_R} + \frac{\gamma-1}{2\gamma}\right]^{\frac{1}{2}} \\ &= r(x,t) - A(p^\star(\xi)) = F(p^\star(\xi)). \end{aligned} \tag{95}$$

Again, the formal iterative procedure (89) can be employed with $\dfrac{\mathrm{d}F(p^\star(\xi))}{\mathrm{d}\xi} = \dfrac{\mathrm{d}F(p^\star(\xi))}{\mathrm{d}p^\star}\dfrac{\mathrm{d}p^\star(\xi)}{\mathrm{d}\xi} = -\dfrac{\mathrm{d}A(p^\star(\xi))}{\mathrm{d}p^\star}\dfrac{\mathrm{d}p^\star(\xi)}{\mathrm{d}\xi}$, where

$$\frac{\mathrm{d}A(p^\star(\xi))}{\mathrm{d}p^\star} = \frac{1}{4}\frac{\gamma+1}{\gamma p_R\sqrt{\frac{(\gamma+1)p^\star(\xi)}{2\gamma p_R} + \frac{\gamma+1}{2\gamma}}}. \tag{96}$$

Let us sketch the reference solution in the plan $\xi - x$ at a final time equal to $t = 0.31$, with the initial position of the diaphragm $x_d = 0.42$ in the figure 20.

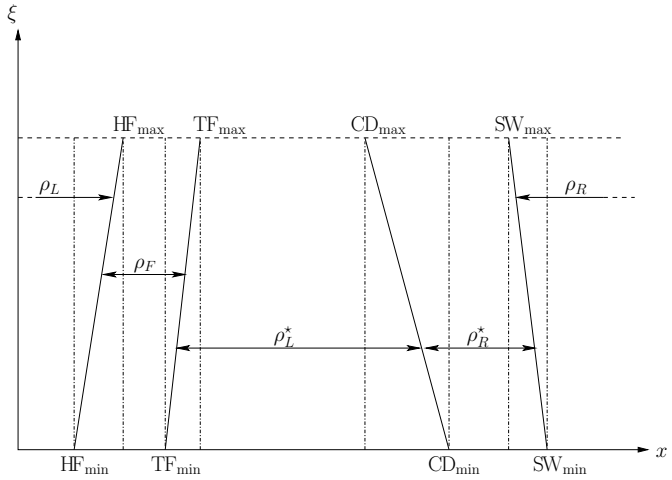

Figure 20. Schematic representation of the density of the uncertain shock tube problem in the combined physical/stochastic space. The regions where the solution should be subdivided are reported with the explicit identification of all the zones defining the variation of the solution as a function of the uncertain parameter ξ.

DOI: 10.1002/fld

The expectation of the-cell averaged physical solution (at time $t = 0.31$) $u(x,\xi,t)$, for each cell $\mathcal{C}_i = [x_i - \frac{|\mathcal{C}_i|}{2}, x_i + \frac{|\mathcal{C}_i|}{2}]$ is computed as follows (here reported explicitly only for the density)

$$\mathcal{E}(\bar{u}_i) = \begin{cases} \dfrac{\rho_L(0)+\rho_L(1)}{2} & \text{if} \quad x_i \le \mathrm{HF}_{\min} \\ \displaystyle\int_0^{\xi_d(x_i)} \rho_F(x,\xi)\mathrm{d}\xi + \rho_L(0)(1-\xi_d(x_i)) + \frac{(\rho_L(1)-\rho_L(0))\,(1-\xi_d^2(x_i))}{2} & \text{if} \quad \mathrm{HF}_{\min} \le x_i \le \mathrm{HF}_{\max} \\ \displaystyle\int_0^1 \rho_F(x,\xi)\mathrm{d}\xi & \text{if} \quad \mathrm{HF}_{\max} \le x_i \le \mathrm{TF}_{\min} \\ \displaystyle\int_0^{\xi_d(x_i)} \rho_L^\star(\xi)\mathrm{d}\xi + \int_{\xi_d(x_i)}^1 \rho_F(x,\xi)\mathrm{d}\xi & \text{if} \quad \mathrm{TF}_{\min} \le x_i \le \mathrm{TF}_{\max} \\ \displaystyle\int_0^1 \rho_L^\star(\xi)\mathrm{d}\xi & \text{if} \quad \mathrm{TF}_{\max} \le x_i \le \mathrm{CD}_{\min} \\ \displaystyle\int_0^{\xi_d(x_i)} \rho_L^\star(\xi)\mathrm{d}\xi + \int_{\xi_d(x_i)}^1 \rho_R^\star(\xi)\mathrm{d}\xi & \text{if} \quad \mathrm{CD}_{\min} \le x_i \le \mathrm{CD}_{\max} \\ \displaystyle\int_0^1 \rho_R^\star(\xi)\mathrm{d}\xi & \text{if} \quad \mathrm{CD}_{\max} \le x_i \le \mathrm{SW}_{\min} \\ \displaystyle\int_0^{\xi_d(x_i)} \rho_R^\star(\xi)\mathrm{d}\xi(1-\xi_d(x_i))\rho_R & \text{if} \quad \mathrm{SW}_{\min} \le x_i \le \mathrm{SW}_{\max} \\ \rho_R & \text{if} \quad x_i \ge \mathrm{SW}_{\max}, \end{cases} \tag{97}$$

where the variance can be computed in a similar way (see what is done for the linear advection equation Section 6.1 and the Burgers equation, Section 6.2. All the numerical quadratures are performed over the stochastic (sub-domain discretized by means of 5000 equally spaced intervals employing a three points Gauss formula:

$$\int_a^b f(\xi)\mathrm{d}\xi = \frac{b-a}{2}\sum_{k=1}^{3} w_k f(\xi_k), \tag{98}$$

where $w_{1,3} = 5/9$, $w_2 = 8/9$, $\xi_{1,3} = \frac{b+a}{2} \pm \frac{b-a}{2}\sqrt{\frac{3}{5}}$ and $\xi_2 = \frac{b+a}{2}$.

REFERENCES

1. Graham I, Kuo F, Nuyens D, Scheichl R, Sloan I. Quasi-Monte Carlo methods for elliptic PDEs with random coefficients and applications. *Journal of Computational Physics* Feb 2011; **230**(10):3668–3694, doi:10.1016/j.jcp.2011.01.023.
2. Babuška I, Nobile F, Tempone R. A Stochastic Collocation Method for Elliptic Partial Differential Equations with Random Input Data. *SIAM Review* 2010; **52**(2):317, doi:10.1137/100786356.
3. Ghanem RG, Spanos PD. *Stochastic Finite Elements. A spectral approach*. Springer Verlag, 1991.
4. Xiu D, Karniadakis GE. Modeling uncertainty in flow simulations via generalized polynomial chaos. *Journal of Computational Physics* May 2003; **187**(1):137–167, doi:10.1016/S0021-9991(03)00092-5.
5. Le Maître O, Knio O. *Spectral Methods for Uncertainty Quantification: With Applications to Computational Fluid Dynamics*. Springer Verlag, 2010.
6. Tryoen J, Le Maître O, Ndjinga M, Ern A. Intrusive Galerkin methods with upwinding for uncertain nonlinear hyperbolic systems q. *Journal of Computational Physics* 2010; **229**:6485–6511.
7. Abgrall R, Congedo PM, Galéra S, Geraci G. Semi-intrusive and non-intrusive stochastic methods for aerospace applications. *4TH EUROPEAN CONFERENCE FOR AEROSPACE SCIENCES, Saint Petersburg, Russia, July 4th-8th, 2011*, 1, 2011; 1–8.
8. Abgrall R, Congedo PM. A semi-intrusive deterministic approach to uncertainty quantifications in non-linear fluid flow problems. *Journal of Computational Physics* 2013; (235):828–845.
9. Abgrall R, Congedo PM, Geraci G. An adaptive multiresolution inspired scheme for solving the stochastic differential equations. *Proceedings of MASCOT 11, 11th Meeting on Applied Scientific Computing and Tools. Grid Generation, Approximation and Visualization. IMACS Series in Computational and Applied Mathematics Vol. 17, IAC - CNR, Rome, Italy*, 2011; 1–10.
10. Abgrall R, Congedo PM, Geraci G, Iaccarino G. Adaptive strategy in multiresolution framework for uncertainty quantification. *Center For Turbulence Research, Prooceedings of the Summer Program 2012*, 2012; 209–218.
11. Abgrall R, Congedo PM, Geraci G. A high-order non-linear multiresolution scheme for stochastic PDEs. *European Workshop on High Order Nonlinear Numerical Methods for Evolutionary PDEs: Theory and Applications (HONOM 2013)*, 2013.

12. Tryoen J. Methodes de Galerkin stochastiques adaptatives pour la propagation d'incertitudes parametriques dans les systemes hyperboliques. PhD Thesis, Univeriste Paris-Est.
13. Tryoen J, Le Maître O, Ern A. Adaptive Anisotropic Spectral Stochastic Methods for Uncertain Scalar Conservation Laws. *SIAM Journal Scientific Computing* 2012; **34**:A2459–A2481.
14. Abgrall R, Congedo PM, Geraci G. A One-Time Truncate and Encode Multiresolution Stochastic Framework. *Technical Report*, INRIA Bordeaux–Sud-Ouest 2012. URL http://hal.inria.fr/index.php?halsid=jbafq4f9vgm551mig8337lnoc4&view_this_doc=hal-00699026&vers
15. Abgrall R, Congedo PM, Geraci G. A One-Time Truncate and Encode Multiresolution Stochastic Framework. *Journal of Computational Physics* 2014; **257**:19–56, doi:http://dx.doi.org/10.1016/j.jcp.2013.08.006.
16. Bellman RE, Richard B. *Adaptive Control Processes: A Guided Tour*. Princeton University Press, 1961.
17. Arandiga F, Donat R. Nonlinear multiscale decompositions: The approach of A. Harten. *Numerical Algorithms* 2000; **23**:175–216.
18. Arandiga F, Chiavassa G, Donat R. Harten framework for multiresolution with applications: From conservation laws to image compression. *Boletín SEMA* 2009; **31**(31):73–108.
19. Abgrall R, Lantéri S, Sonar T. ENO approximations for compressible fluid dynamics. *ZAMM Z Angew. Math. Mech.* 1999; **79**(1):3–28. URL http://onlinelibrary.wiley.com/doi/10.1002/(SICI)1521-4001(199901)79:1%3C3::AID-ZAMM3%3E3.0.CO;
20. Jiang G, Shu CW. Efficient implementation of weighted ENO schemes. *Journal of Computational Physics* 1996; **228**(126):202–228. URL http://oai.dtic.mil/oai/oai?verb=getRecord&metadataPrefix=html&identifier=ADA3
21. Aràndiga F, Belda AM. Weighted ENO interpolation and applications. *Communications in Nonlinear Science and Numerical Simulation* Apr 2004; **9**(2):187–195.
22. Harten A. Adaptive multiresolution schemes for shock computations. *Journal of Computational Physics* Aug 1994; **135**(2):260–278.
23. Harten A. Multiresolution algorithms for the numerical solution of hyperbolic conservation laws. *Communications on Pure and Applied Mathematics* 1995; **48**(12):1305–1342.
24. Harten A. Discrete multi-resolution analysis and generalized wavelets. *Applied Numerical Mathematics* 1993; **12**(13):153 – 192.
25. Abgrall R, Harten A. Multiresolution Representation in Unstructured Meshes. *SIAM Journal on Numerical Analysis* 1998; **35**(6):2128–2146.
26. Getreuer P, Meyer FG. ENO multiresolutions Schemes with General Discretizations. *SIAM Journal on Numerical Analysis* 2008; **46**(6):2953–2977.
27. Abgrall R, Sonar T. On the use of Mühlbach expansions in the recovery step of ENO methods. *Numerische Mathematik* 1997; (1997):1–25.
28. Daubechies I. *Ten Lectures on Wavelets*. CBMS-NSF Regional Conference Series in Applied Mathematics.
29. Quarteroni A, Sacco R, Saleri F. *Matematica Numerica*. Springer, 2008.
30. Abgrall R. On Essentially Non-oscillatory Schemes on Unstructured Meshes: Analysis and Implementation. *Journal of Computational Physics* Sep 1994; **114**(1):45–58.
31. LeVeque RJ. *Finite volume methods for conservation laws and hyperbolic systems*. Cambridge University Press, 2002.
32. Toro EF. *Riemann solvers and numerical methods for fluid mechanics*. Springer, Berlin, 1997.
33. Holtz M. Sparse Grid Quadrature in High Dimensions with Applications in Finance and Insurance. PhD Thesis 2008.
34. Sod G. Finite Difference Methods for Systems of Nonlinear Hyperbolic Conservation Laws. *Journal of Computational Physics* 1978; (27):1–31.